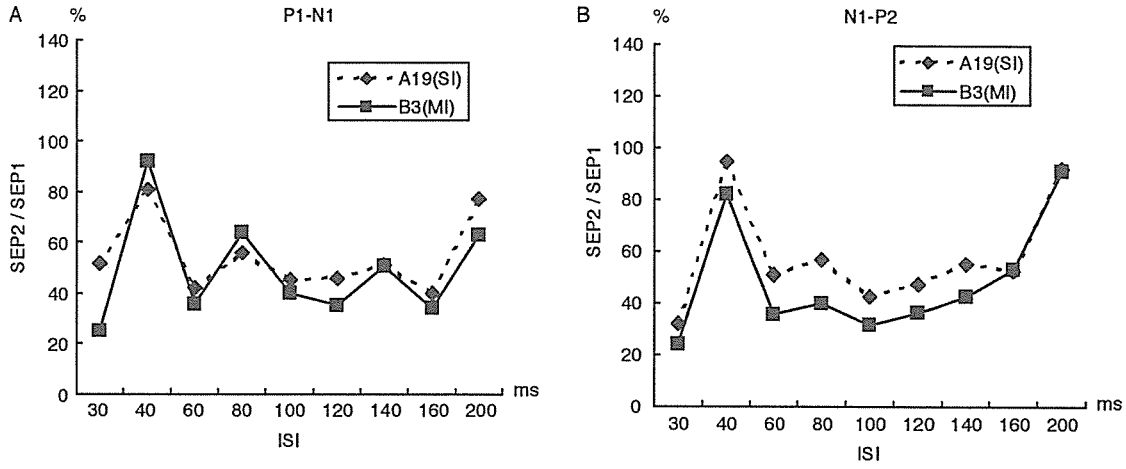

Fig. 3. Recovery curve of P1–N1 (A) and N1–P2 (B) components of the subdurally recorded SEP amplitude in the paired pulse stimulation paradigm. Dotted lines; recovery curve at A19 (SI), solid lines; recovery curve at B3 (MI). The second response was significantly less suppressed at ISIs of 40 and 200 ms, as compared with other ISIs, for P1–N1 and N1–P2 components both at SI and MI.

suppression of SEP 2 at ISIs of 40 and 200 ms (labeled as less suppressed) was significantly different as compared with that of other ISIs (labeled as suppressed) (P1–N1 component: $P=0.004$, N1–P2 component: $P=0.003$).

4. Discussion

With regard to the upper limb stimulation, Cowan et al. recorded intraoperative epicortical giant SEPs under general anesthesia (Cowan et al., 1986). They showed that the latency and polarity of the SEP waveforms, recorded from the cortex apparently posterior to the postcentral gyrus, were similar to those of the scalp recorded ones, although EEG and electrocorticogram (ECoG) were not simultaneously recorded (Cowan et al., 1986). However, there was no previous report of giant SEPs recorded while awake, and furthermore, no studies recorded directly from SI and MI simultaneously. To our knowledge, this is the clear invasive recording of giant SEPs at both SI and MI following lower limb stimulation in an awake patient with cortical reflex myoclonus, and thus it enables us to investigate at least a part of the mechanism underlying generation of cortical reflex myoclonus. However, we should consider two technical limitations in this study. First, some part of the left foot/leg SMI was not covered by the subdural electrodes. Second, the influence of cortical dysplasia or epileptic hyperexcitability on giant SEP generation could not be excluded.

Giant SEPs recorded from SI and MI were similar in morphology. These findings indicate that both SI and MI are hyperexcitable to somatosensory stimuli. The fact that the peaks at SI always occurred earlier than those at MI by about 6 ms suggests that, in the present patient, enhanced response to somatosensory input initially occurred in SI due to its own hyperexcitability, and subsequently the impulse is conducted to MI. The delay of 6 ms seems consistent with cortico-cortical conduction time, since conduction time of a similar duration have been recorded between different muscles within MI in cortical myoclonus (Brown et al., 1991).

Therefore, giant SEPs in this patient are composed of two components; one due to SI hyperexcitability causing giant response to the somatosensory input, and the other arising from MI hyperexcitability most likely induced by the input from SI. This hyperexcitability enhanced by SI, in the present patient, was supported by the fact that SI was the most usual source of the pre-myoclonus spike in patients with cortical reflex myoclonus (Uesaka et al., 1996), but it may not completely exclude the possibility that MI itself is hyperexcitable. Although there is a direct input from the thalamus to the motor cortices and MI alone could also be the source of the pre-myoclonus spike in some patients with cortical myoclonus (Terao et al., 1997; Uesaka et al., 1996), the present findings do not suggest the role of this system at least in the present case. Previous magnetoencephalographic (MEG) study on cortical reflex myoclonus suggested the hyperexcitability of both SI and MI, but the time difference between SI and MI was not clearly delineated (Mima et al., 1998). It may be explained by the limited sensitivity of MEG as compared with epicortical recording or by the different etiology between the two disease groups.

The similar morphology of early components of giant SEPs between scalp and epicortical recording is consistent with the previous upper limb study (Cowan et al., 1986). However, the peaks P1 and N1 occurred consistently earlier at subdural SI than over the scalp by 4.3–11.1 ms. It could be explained, at least partly, by the phase shift of about 8 ms as the effect of skull bone which could behave as the 15 Hz high frequency filter (Tyner et al., 1983). On the other hand, P1 and N1 peaks at subdural MI were similar to those at scalp recording. Foot MI was buried in the mesial surface whereas foot SI was exposed both on the lateral and mesial surfaces as shown in Fig. 1C. Taken together with the skull bone effect as described above, it is postulated that scalp recorded P1 and N1 reflect those arising from SI rather than MI in the present

patient. In contrast, the morphology of the late components (including P2) of giant SEPs was not identical between the scalp EEG and the ECoG. It may be explained by the different position of reference electrodes and different ISI employed between the scalp and ECoG recording (the former adopted linked earlobes as the reference and ISI of 2.9 s, and the latter left mastoid process and 1 s).

The similarity in latencies between SEPs and SEFs was also observed in previous study (Mima et al., 1998). This result could be partly explained by the characteristics of MEG because MEG signals usually reflect the cortical activities that are derived from the intracellular current tangentially oriented to the scalp.

Kakigi and Shibasaki reported giant SEPs in response to tibial nerve stimulation in 3 patients with cortical reflex myoclonus due to various causes (progressive myoclonic epilepsy, sialidosis and uremic encephalopathy) (Kakigi and Shibasaki, 1987b). They showed enhanced P1–N1 components localized maximum at Cz or CPz. Their findings are consistent with our scalp SEPs in terms of amplitude. In their study, one patient showed delayed P1 and N1 components, as seen in our patient.

Paired SEPs demonstrated that the SEP2 was less suppressed, as compared with other ISIs, both at SI and MI for the ISIs of 40 and 200 ms. Decreased inhibition around ISI 40 ms was similar to the previous upper limb studies (Shibasaki et al., 1985; Ugawa et al., 1991). This consistent result between upper and lower limb giant SEPs indicates the mechanism of disinhibition at ISI of 40 ms which could be explained by the intracortical factors after the somatosensory afferent signals reach the SI. It could correlate with exaggerated scalp recorded 16–20 Hz (interval of 42–50 ms) oscillatory EEG potentials over the contralateral SMI in patients with positive or negative myoclonus (Ugawa et al., 2003). On the other hand, disinhibition at ISI of 200 ms could be explained by the earlier recovery usually almost completed at ISI of 300 ms in normal subjects (Ugawa et al., 1991). SEP2 was suppressed by the preceding stimulus (SEP1) to a lesser degree, as compared with other ISIs, but it was still less than 100% of the SEP1 at ISIs of 40 and 200 ms, as opposed to more than 100% of SEP1 in the previous studies (Shibasaki et al., 1985; Ugawa et al., 1991). It may be explained by the fact that the present patient was treated by many kinds of anticonvulsants that could enhance inhibitory activity within the brain. The effect of anticonvulsants and epileptic activity on the result of single pulse as well as paired pulse SEPs remains to be taken into consideration.

Acknowledgements

This study was supported by the Research Grant for the Treatment of Intractable Epilepsy (16-1) from the Japan Ministry of Health, Labor and Welfare, the Scientific Research Grant (C2) 18590935 from the Japan Society for the Promotion of Science (JSPS), Nakayama Foundation for Human Science, the Grants-in-Aid for Young Scientists (B) 17790578 from the Japan Ministry of Education, Culture, Sports, Science and Technology (MEXT), Kanae Foundation for life and socio-medical science.

References

Brown P, Day BL, Rothwell JC, Thompson PD, Marsden CD. Intrahemispheric and interhemispheric spread of cerebral cortical myoclonic activity and its relevance to epilepsy. Brain 1991;114:2333–51.

Cowan JM, Rothwell JC, Wise RJ, Marsden CD. Electrophysiological and positron emission studies in a patient with cortical myoclonus, epilepsia partialis continua and motor epilepsy. J Neurol Neurosurg Psychiatry 1986;49:796–807.

Hitomi T, Ikeda A, Matsumoto R, Kinoshita M, Taki J, Usui K, Mikuni N, Nagamine T, Hashimoto N, Shibasaki H. Subdural recording of giant somatosensory evoked potentials (SEPs): a comparison between primary motor (MI) and sensory cortex (SI) (abstract). Eighth international evoked potentials symposium; 2004. p. 416.

Ikeda A, Shibasaki H, Nagamine T, Xu X, Terada K, Mima T, Kaji R, Kawai I, Tatsuoka Y, Kimura J. Peri-rolandic and fronto-parietal components of scalp-recorded giant SEPs in cortical myoclonus. Electroencephalogr Clin Neurophysiol 1995;96:300–9.

Kakigi R, Shibasaki H. Generator mechanisms of giant somatosensory evoked potentials in cortical reflex myoclonus. Brain 1987a;110:1359–73.

Kakigi R, Shibasaki H. Somatosensory evoked potentials following stimulation of the lower limb in cortical reflex myoclonus. J Neurol Neurosurg Psychiatry 1987b;50:1641–6.

Matsumoto R, Kinoshita M, Taki J, Hitomi T, Mikuni N, Shibasaki H, Fukuyama H, Hashimoto N, Ikeda A. In vivo epileptogenicity of focal cortical dysplasia: a cortical paired stimulation study. Epilepsia 2005; 46:1744–9.

Mikuni N, Ikeda A, Yoneko H, Amano S, Hanakawa T, Fukuyama H, Hashimoto N. Surgical resection of an epileptogenic cortical dysplasia in the deep foot sensorimotor area. Epilepsy Behav 2005;7(3):559–62.

Mima T, Nagamine T, Nishitani N, Mikuni N, Ikeda A, Fukuyama H, Takigawa T, Kimura J, Shibasaki H. Cortical myoclonus: sensorimotor hyperexcitability. Neurology 1998;50:933–42.

Nakagawa Y, Matsumoto R, Ikeda A, Mikuni N, Matsuhashi M, Hanakawa T, Fukuyama H, Shimohama S. Focal cortical dysplasia at the primary somatosensory cortex could manifest both intractable partial epilepsy and cortical reflex myoclonus. Clin Neurol (Tokyo) (only abstract in English), in press.

Shibasaki H, Yamashita Y, Neshige R, Tobimatsu S, Fukui R. Pathogenesis of giant somatosensory evoked potentials in progressive myoclonic epilepsy. Brain 1985;108:225–40.

Shibasaki H, Nakamura M, Nishida S, Kakigi R, Ikeda A. Wave form decomposition of 'giant SEP' and its computer model for scalp topography. Electroencephalogr Clin Neurophysiol 1990;77:286–94.

Terao Y, Ugawa Y, Hanajima R, Yumoto M, Kawahara Y, Yamamoto T, Shirouzu I, Kanazawa I. Motor cortical reflex myoclonus: a case study with MEG. Electroencephalogr Clin Neurophysiol 1997;102:505–11.

Tyner FS, Knott JR, Mayer Jr WB. Fundamentals of EEG technology, vol. 1; 1983. p. 49–50.

Uesaka Y, Terao Y, Ugawa Y, Yumoto M, Hanajima R, Kanazawa I. Magnetoencephalographic analysis of cortical myoclonic jerks. Electroencephalogr Clin Neurophysiol 1996;99:141–8.

Ugawa Y, Genba K, Shimpo T, Mannen T. Somatosensory evoked potential recovery (SEP-R) in myoclonic patients. Electroencephalogr Clin Neurophysiol 1991;80:21–5.

Ugawa Y, Hanajima R, Terao Y, Kanazawa I. Exaggerated 16–720 Hz motor cortical oscillation in patients with positive or negative myoclonus. Clin Neurophysiol 2003;114:1278–84.

Acta Crystallographica Section F
Structural Biology
and Crystallization
Communications
ISSN 1744-3091

Structure of human ubiquitin-conjugating enzyme E2 G2 (UBE2G2/UBC7)

Ryoichi Arai,[a,b]‡ Seiko Yoshikawa,[a]‡ Kazutaka Murayama,[a,c] Yuzuru Imai,[d] Ryosuke Takahashi,[d,e] Mikako Shirouzu[a,b] and Shigeyuki Yokoyama[a,b,f]*

[a]Protein Research Group, RIKEN Genomic Sciences Center, Tsurumi, Yokohama 230-0045, Japan, [b]RIKEN SPring-8 Center, Harima Institute, Sayo, Hyogo 679-5148, Japan, [c]Tohoku University Biomedical Engineering Research Organization, Aoba, Sendai 980-8575, Japan, [d]RIKEN Brain Science Institute, Wako, Saitama 351-0198, Japan, [e]Department of Neurology, Graduate School of Medicine, Kyoto University, Sakyo, Kyoto 606-8507, Japan, and [f]Department of Biophysics and Biochemistry, Graduate School of Science, The University of Tokyo, Bunkyo, Tokyo 113-0033, Japan

‡ These authors contributed equally to this work.

Correspondence e-mail: yokoyama@biochem.s.u-tokyo.ac.jp

Received 22 December 2005
Accepted 10 March 2006

PDB Reference: human UBE2G2/UBC7, 2cyx, r2cyxsf.

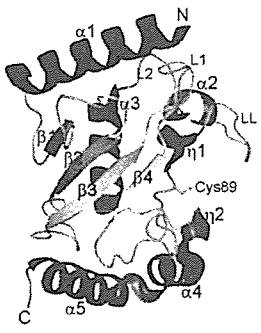

The human ubiquitin-conjugating enzyme E2 G2 (UBE2G2/UBC7) is involved in protein degradation, including a process known as endoplasmic reticulum-associated degradation (ERAD). The crystal structure of human UBE2G2/UBC7 was solved at 2.56 Å resolution. The UBE2G2 structure comprises a single domain consisting of an antiparallel β-sheet with four strands, five α-helices and two 3_{10}-helices. Structural comparison of human UBE2G2 with yeast Ubc7 indicated that the overall structures are similar except for the long loop region and the C-terminal helix. Superimposition of UBE2G2 on UbcH7 in a c-Cbl–UbcH7–ZAP70 ternary complex suggested that the two loop regions of UBE2G2 interact with the RING domain in a similar way to UbcH7. In addition, the extra loop region of UBE2G2 may interact with the RING domain or its neighbouring region and may be involved in the binding specificity and stability.

1. Introduction

Ubiquitin-dependent protein degradation plays an important role in the regulation of various cellular processes, including cell-cycle progression, signal transduction, transcription, DNA repair and protein quality control (Koepp *et al.*, 1999; Laney & Hochstrasser, 1999). Ubiquitination involves the successive actions of the ubiquitin-activating (E1), ubiquitin-conjugating (E2) and ubiquitin-protein ligase enzymes (E3) (Hershko & Ciechanover, 1998; Pickart, 2001). The E1 enzyme activates free ubiquitin and transfers it to E2 through a thioester linkage between the ubiquitin C-terminus and an E2 active-site cysteine. The E3 enzyme recognizes its substrate and E2 and catalyzes the formation of an isopeptide bond between a lysine ε-amino group of the substrate (or ubiquitin) and the C-terminal carboxyl group of ubiquitin Gly76. Over 30 human E2s have been identified and they all contain a conserved ~150 amino-acid catalytic core. The E2 enzymes are grouped into four classes depending on the presence and the location of additional sequences (Jentsch, 1992). Some of these enzymes contain extra C-terminal and/or N-terminal extensions from the core domain. The class I enzymes are the smallest E2 enzymes and consist almost entirely of the conserved core domain. The class II enzymes contain an extra C-terminal extension from the core domain, while class III enzymes have an N-terminal extension. The class IV enzymes contain both N- and C- terminal extensions.

The human UBE2G2 gene encodes the ubiquitin-conjugating enzyme E2 G2 (UBE2G2/UBC7), with a molecular weight of 18.6 kDa (165 amino acids). It was mapped to the region of human chromosome 21q22.3 and its transcripts are ubiquitously expressed in human tissues (Katsanis & Fisher, 1998; Rose *et al.*, 1998). Human UBE2G2 is a class I E2 enzyme. Recently, bacterial expression of His-tagged human UBE2G2 was reported (Reyes *et al.*, 2006). The human UBE2G2 protein shares 100, 62, 47 and 27% identities to murine UBE2G2/UBC7 (MmUBC7), yeast Ubc7, human UBE2G1 and human UbcH7, respectively (Fig. 1*a*). The crystal structures of yeast Ubc7 (Cook *et al.*, 1997), a human E6AP–UbcH7 complex (Huang *et*

al., 1999) and a human c-Cbl–UbcH7–ZAP-70 complex (Zheng *et al.*, 2000) have been reported. Functional studies have associated yeast Ubc7 and MmUBC7 with the degradation of endoplasmic reticulum (ER) substrates, a process known as ER-associated degradation (ERAD; Jungmann *et al.*, 1993; Fang *et al.*, 2001; Tiwari & Weissman, 2001). Parkin, a gene product responsible for autosomal recessive juvenile Parkinsonism (AR-JP), interacts with human UBE2G2/UBC7 and UBC6 through its RING domain and specifically ubiquitinates the Pael receptor in the presence of the E2s (Imai *et al.*, 2001). Furthermore, exogenous MmUBC7 mediates the ubiquitination and down regulation of both the inositol 1,4,5-triphosphate receptor in human neuroblastoma cells (Webster *et al.*, 2003) and the human type 2 iodothyronine selenodeiodinase (Kim *et al.*, 2003). Recently, the interactions of human UBE2G2/UBC7 with some RING-finger E3s, such as human HRD1 (Kikkert *et al.*, 2004) and TEB4 (Hassink *et al.*, 2005), have been reported. To analyze the structural and functional details of human UBE2G2/UBC7, which is involved in important cellular processes, its structure must be determined and compared with those of its homologues. Here, we report the crystal structure of human UBE2G2/UBC7 at 2.56 Å resolution and discuss its structural aspects.

2. Materials and methods

2.1. Protein expression and purification

The human UBE2G2 gene (Imai *et al.*, 2001) encoding human ubiquitin-conjugating enzyme E2 G2 (UBE2G2/UBC7) was cloned into a modified pENTR vector with a tobacco etch virus (TEV) protease cleavage site, derived from pENTR1A (Invitrogen). The expression vector pET/cMBP-UBE2G2 was constructed using Gateway technology (Invitrogen) with pENTR/TEV-UBE2G2 and pET/cMBP-GATEWAY bearing a T7 promoter, an N-terminal maltose-binding protein (MBP) tag and a Gateway reading frame cassette A (Invitrogen). The UBE2G2 protein was expressed as a fusion with an N-terminal MBP tag and a TEV protease cleavage site in *Escherichia coli* BL21(DE3). The protein was first purified on an amylose-resin column (New England Biolabs) and the MBP tag was then cleaved by His-tagged TEV protease, which was removed using a HisTrap column (GE Healthcare). The protein was purified further by Mono-Q and Superdex 75 column (GE Healthcare) chromatography steps. The yield of purified UBE2G2 protein was 8 mg per litre of culture. The construct that was used for crystallization contained the cloning artifact sequence GGSEF at the N-terminus.

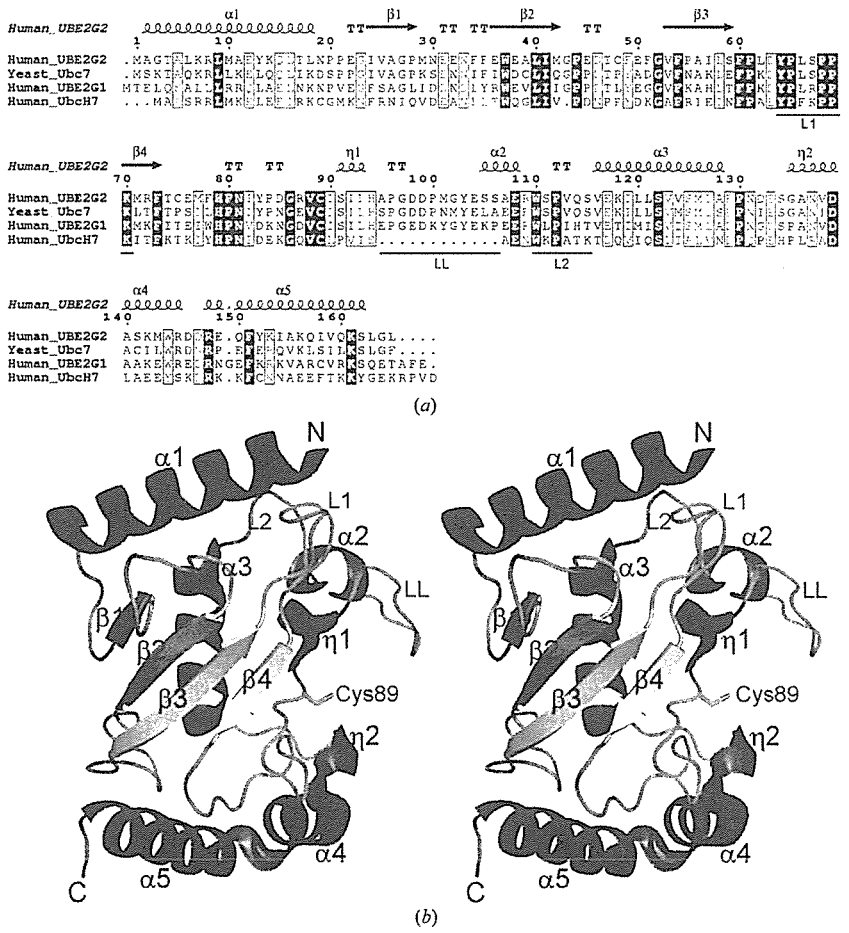

Figure 1
(*a*) Sequence alignment of homologues of human UBE2G2/UBC7. The alignment was generated by *ESPript* (Gouet *et al.*, 1999) with *CLUSTAL W* (Thompson *et al.*, 1994). The secondary structures of the human UBE2G2 protein, as determined by *DSSP* (Kabsch & Sander, 1983), are shown above the sequences (α, α-helix; β, β-strand; η, 3_{10}-helix; TT, β-turn). (*b*) Ribbon representation of the human UBE2G2/UBC7 structure (amino acids 1–165; stereoview). The helices and the β-strands are shown in red and yellow, respectively. The active-site residue (Cys89) is shown as a stick model.

2.2. Crystallization and data collection

Preliminary crystals of human UBE2G2 were obtained under condition No. 42 (0.1 *M* Tris–HCl buffer pH 8.5 containing 1.5 *M* ammonium sulfate and 12% glycerol) of the Crystal Screen 2 crystal screening kit (Hampton Research) using the 96-well sitting-drop vapour-diffusion method. The crystals of UBE2G2 used for structure determination were obtained in drops composed of 1 µl 8.5 mg ml^{-1} protein solution (20 m*M* Tris–HCl buffer pH 8.0 containing 120 m*M* NaCl, 2 m*M* DTT) and 1 µl reservoir solution (0.1 *M* Tris–HCl buffer pH 8.1 containing 1.45 *M* ammonium sulfate and 12% glycerol; Hampton Research) by the hanging-drop vapour-diffusion method against 500 µl reservoir solution. A rod-like crystal (~350 × 100 × 100 µm) was obtained within a few days and was used for data collection. The data collection was carried out at 100 K, with the reservoir solution containing 27.5% glycerol as a cryoprotectant. The diffraction data were collected at SPring-8 BL26B1 (Yamamoto *et al.*, 2002) and were recorded on a Jupiter 210 CCD detector (Rigaku). All diffraction data were processed with the *HKL*2000 program suite (Otwinowski & Minor, 1997).

2.3. Structure determination and refinement

The structure was solved by the molecular-replacement method using *MOLREP* (Vagin & Teplyakov, 1997) with the yeast Ubc7 structure (PDB code 2ucz; Cook *et al.*, 1997) as a search model. Data in the resolution range 50–3.0 Å were used in both rotation and translation calculations, which gave an obvious solution with significant contrast, resulting in three molecules in the asymmetric unit with a Matthews coefficient (V_M) of 3.83 Å^3 Da^{-1} and a solvent content of 67.91%. The model was corrected iteratively using *O* (Jones *et al.*, 1991) and was refined to 2.56 Å using *LAFIRE* (Yao *et al.*, 2006), *REFMAC5* (Murshudov *et al.*, 1997) and *Crystallography & NMR System* (*CNS*; Brünger *et al.*, 1998). The crystallographic data and refinement statistics are presented in Table 1. Since there was additional electron density, four residues of the cloning artifact sequence at the N-terminus were also modelled. The final model includes 507 amino-acid residues of three UBE2G2 monomers and 23 water molecules in the asymmetric unit. In the loop regions (residues 100–106 and 131–133), the electron density corresponding to the side chains was ambiguous, which increased the *B* factor. In addition, relatively large areas of the molecular surface were exposed to the solvent in the crystal as the solvent content was high. These features resulted in the high average *B* factor. The quality of the model was inspected using *PROCHECK* (Laskowski *et al.*, 1993). The figures were created using *PyMOL* (DeLano, 2005).

Table 1
X-ray data-collection and refinement statistics.

Values in parentheses are for the outer shell (2.65–2.56 Å).

Data collection	
Space group	$P2_12_12_1$
Unit-cell parameters (Å)	a = 63.52, b = 87.61, c = 157.41
Wavelength (Å)	1.000
Resolution (Å)	50–2.56
Total reflections	117935
Unique reflections	28705
Redundancy	4.1 (3.7)
Completeness (%)	97.5 (84.6)
$I/\sigma(I)$	22.2 (4.2)
R_{sym}† (%)	5.5 (29.3)
Refinement	
Resolution (Å)	49.43–2.56
No. of reflections	28395
No. of protein atoms	3996
No. of water molecules	23
R_{work} (%)	22.8
R_{free}‡ (%)	26.2
R.m.s.d. bond lengths (Å)	0.009
R.m.s.d. bond angles (°)	1.6
Average *B* factor (Å^2)	75.7
Ramachandran plot	
Most favoured regions (%)	85.9
Additional allowed regions (%)	14.1
Generously allowed regions (%)	0.0
Disallowed regions (%)	0.0

† $R_{sym} = \sum|I_i - I_{avg}|/\sum I_i$, where I_i is the observed intensity and I_{avg} is the average intensity. ‡ R_{free} is calculated for 10% of randomly selected reflections excluded from refinement.

3. Results and discussion

The crystal structure of human UBE2G2 comprises a single domain consisting of an antiparallel β-sheet with four strands (β1–β4), five α-helices (α1–α5) and two 3_{10}-helices (η1 and η2; Fig. 1*b*). The ubiquitin-accepting residue Cys89 is located near η1. The overall folding of UBE2G2 corresponds to the typical fold of ubiquitin-conjugating enzymes. According to analytical ultracentrifugation, the

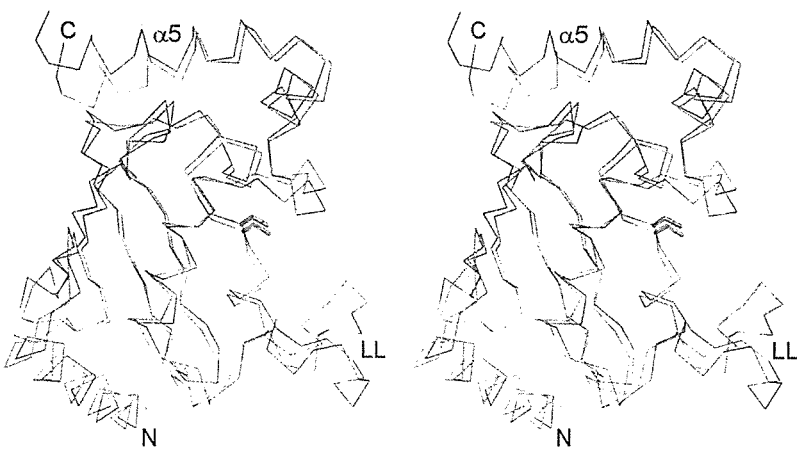

Figure 2
Superimposition of the main-chain structures of human UBE2G2 (green) and yeast Ubc7 (orange) (PDB code 2ucz; Cook *et al.*, 1997) (stereoview). The active-site cysteine residues are shown as stick models. The superimposition was carried out with *LSQKAB* (Kabsch, 1976).

molecular weight of UBE2G2 was ~18 kDa (data not shown), indicating that the UBE2G2 protein exists as a monomer in solution.

Fig. 2 shows the superimposition of the main-chain structures of human UBE2G2 and yeast Ubc7 (Cook *et al.*, 1997). The overall structure of UBE2G2 is remarkably similar to that of yeast Ubc7 (r.m.s.d. = 2.15 Å over 164 C^{α} atoms). The major differences between human UBE2G2 and yeast Ubc7 are the structure of the long loop (LL) region (95–106) and the angle of the C-terminal helix. The C-terminal helix (α5) of UBE2G2 is closer to the β-sheet core region than that of yeast Ubc7. The important interactions of UBE2G2 in the contact region of the C-terminal helix and the core region are the hydrophobic interactions among Phe54, Met77, Phe78, Ile154 and Ile158 and the salt bridge between Glu76 and Lys161. The residues Glu76, Ile154 and Ile158 are replaced with Ser76, Gln154 and Ser158 in yeast Ubc7, respectively, suggesting that the interactions of yeast Ubc7 are weaker than those of UBE2G2. Consequently, the angle of the C-terminal helix (α5) may change. Recently, the crystal structure of the human ubiquitin-conjugating enzyme E2 G1 (UBE2G1), which is another human homologue of yeast Ubc7, was deposited in the PDB (PDB code 2awf). A structural comparison of UBE2G2 with UBE2G1 revealed that the overall folding of UBE2G2 is similar to that of UBE2G1 (r.m.s.d. = 1.12 Å over 115 C^{α} atoms), but in UBE2G1 the residues 98–106 within the long loop (LL) region and the C-terminal helices (η2, α4 and α5) were not located in the model owing to disorder.

Zheng and coworkers reported the crystal structure of a c-Cbl–UbcH7–ZAP70 peptide ternary complex (PDB code 1fbv; Zheng *et al.*, 2000). It revealed how the RING domain of c-Cbl recruits the ubiquitin-conjugating enzyme UbcH7. Fig. 3(*a*) shows the superimposition of the main-chain structures of UBE2G2 and UbcH7 in the ternary complex. The overall folding of UBE2G2 and UbcH7 overlaps roughly (r.m.s.d. = 2.95 Å over 143 C^{α} atoms). Fig. 3(*b*) shows a close-up view of the interface between the RING domain and the E2s. The critical residues of UbcH7 for the interaction with the RING domain, Pro62, Phe63, Lys96, Pro97 and Ala98 (Zheng *et al.*, 2000), and the corresponding residues of UBE2G2, Pro65, Leu66,

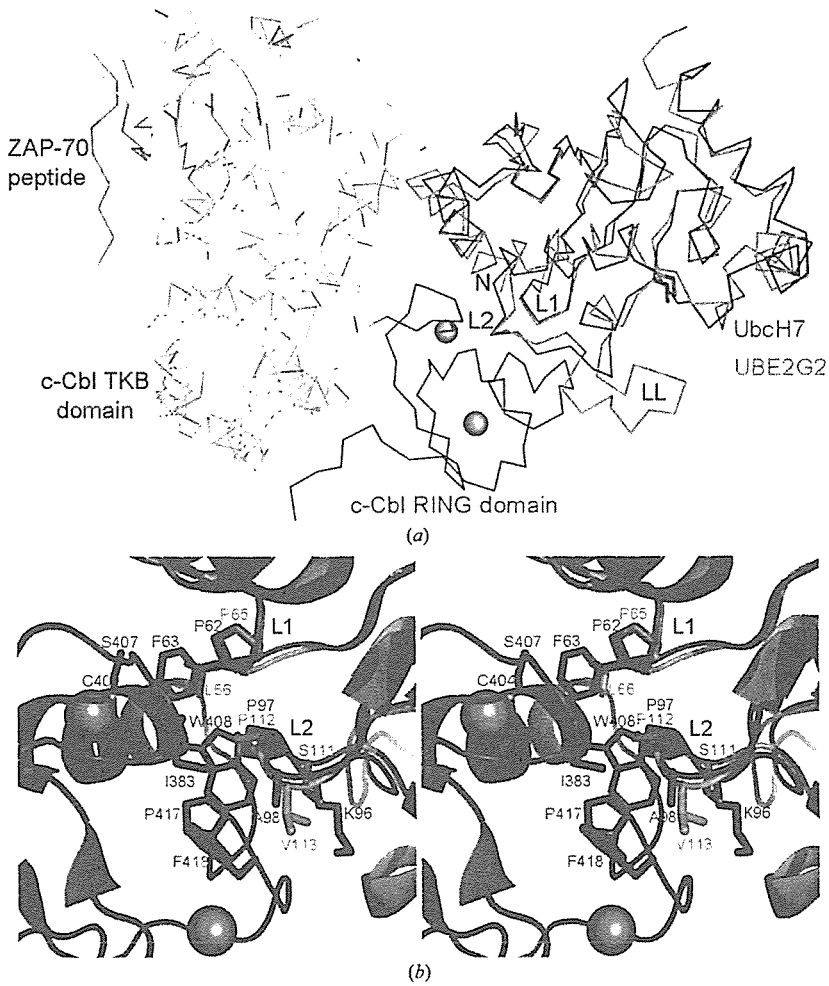

Figure 3
(*a*) Superimposition of the main-chain structures of human UBE2G2 and UbcH7 in the c-Cbl–UbcH7–ZAP70 peptide ternary complex (PDB code 1fbv; Zheng *et al.*, 2000). The TKB domain and linker sequence of c-Cbl, the RING domain of c-Cbl, the ZAP-70 peptide and human UbcH7 are coloured yellow, red, cyan and magenta, respectively. The zinc ions are indicated by grey spheres. The human UBE2G2 protein is coloured green. The active-site cysteine residues are shown as stick models. (*b*) Close-up view of the ribbon representation of the interface between the RING domain and UbcH7 in the c-Cbl–UbcH7–ZAP70 complex and the superimposition of UBE2G2 on UbcH7 (stereoview). The colouring is the same as that in Fig. 3(*a*). The critical residues for the interaction of UbcH7 with the *RING* domain and the corresponding residues of UBE2G2 are shown as stick models. All superimpositions were carried out with *LSQKAB* (Kabsch, 1976).

Ser111, Pro112 and Val113, overlap remarkably well (r.m.s.d. = 0.768 Å over five C^{α} atoms), suggesting that the L1 (64–70) and L2 (110–115) loops of UBE2G2 are involved in the interaction with the RING domain in a similar way as UbcH7. This is consistent with the previous results that Parkin binds to UBE2G2 as well as UbcH7 and ubiquitinates substrates (Imai *et al.*, 2000, 2001). In addition, UBE2G2 has the extra long loop (LL) region (95–106), which is probably located on the side near the RING domain. The *B* factor of the LL region is relatively high, implying the possibility of conformational flexibility. The LL region may interact with the RING domain or its neighbouring region and may be involved in the binding specificity and stability.

We thank Mr R. Akasaka and Dr M. Kukimoto-Niino for the analytical ultracentrifugation, Mr S. Kamo for computer maintenance and Ms A. Ishii, Ms K. Yajima, Ms M. Sunada and Ms T. Nakayama for clerical assistance. We also thank Dr M. Yamamoto for data collection at the RIKEN Structural Genomics beamline BL26B1 at SPring-8. This work was supported by the RIKEN Structural Genomics/Proteomics Initiative (RSGI), the National Project on Protein Structural and Functional Analyses, the Ministry of Education, Culture, Sports, Science and Technology of Japan.

References

Brünger, A. T., Adams, P. D., Clore, G. M., DeLano, W. L., Gros, P., Grosse-Kunstleve, R. W., Jiang, J.-S., Kuszewski, J., Nilges, M., Pannu, N. S., Read, R. J., Rice, L. M., Simonson, T. & Warren, G. L. (1998). *Acta Cryst.* D**54**, 905–921.

Cook, W. J., Martin, P. D., Edwards, B. F., Yamazaki, R. K. & Chau, V. (1997). *Biochemistry*, **36**, 1621–1627.

DeLano, W. L. (2005). *PyMOL* v.0.98. DeLano Scientific, South San Francisco, CA, USA.

Fang, S., Ferrone, M., Yang, C., Jensen, J. P., Tiwari, S. & Weissman, A. M. (2001). *Proc. Natl Acad. Sci. USA*, **98**, 14422–14427.

Gouet, P., Courcelle, E., Stuart, D. I. & Metoz, F. (1999). *Bioinformatics*, **15**, 305–308.

Hassink, G., Kikkert, M., van Voorden, S., Lee, S. J., Spaapen, R., van Laar, T., Coleman, C. S., Bartee, E., Fruh, K., Chau, V. & Wiertz, E. (2005). *Biochem. J.* **388**, 647–655.

Hershko, A. & Ciechanover, A. (1998). *Annu. Rev. Biochem.* **67**, 425–479.

Huang, L., Kinnucan, E., Wang, G., Beaudenon, S., Howley, P. M., Huibregtse, J. M. & Pavletich, N. P. (1999). *Science*, **286**, 1321–1326.

Imai, Y., Soda, M., Inoue, H., Hattori, N., Mizuno, Y. & Takahashi, R. (2001). *Cell*, **105**, 891–902.

Imai, Y., Soda, M. & Takahashi, R. (2000). *J. Biol. Chem.* **275**, 35661–35664.

Jentsch, S. (1992). *Annu. Rev. Genet.* **26**, 179–207.

Jones, T. A., Zou, J. Y., Cowan, S. W. & Kjeldgaard, M. (1991). *Acta Cryst.* A**47**, 110–119.

Jungmann, J., Reins, H. A., Schobert, C. & Jentsch, S. (1993). *Nature (London)*, **361**, 369–371.

Kabsch, W. (1976). *Acta Cryst.* A**32**, 922–923.

Kabsch, W. & Sander, C. (1983). *Biopolymers*, **22**, 2577–2637.

Katsanis, N. & Fisher, E. M. (1998). *Genomics*, **51**, 128–131.

Kikkert, M., Doolman, R., Dai, M., Avner, R., Hassink, G., van Voorden, S., Thanedar, S., Roitelman, J., Chau, V. & Wiertz, E. (2004). *J. Biol. Chem.* **279**, 3525–3534.

Kim, B. W., Zavacki, A. M., Curcio-Morelli, C., Dentice, M., Harney, J. W., Larsen, P. R. & Bianco, A. C. (2003). *Mol. Endocrinol.* **17**, 2603–2612.

Koepp, D. M., Harper, J. W. & Elledge, S. J. (1999). *Cell*, **97**, 431–434.

Laney, J. D. & Hochstrasser, M. (1999). *Cell*, **97**, 427–430.

Laskowski, R. A., MacArthur, M. W., Moss, D. S. & Thornton, J. M. (1993). *J. Appl. Cryst.* **26**, 283–291.

Murshudov, G. N., Vagin, A. A. & Dodson, E. J. (1997). *Acta Cryst.* D**53**, 240–255.

Otwinowski, Z. & Minor, W. (1997). *Methods Enzymol.* **276**, 307–326.

Pickart, C. M. (2001). *Annu. Rev. Biochem.* **70**, 503–533.

Reyes, L. F., Sommer, C. A., Beltramini, L. M. & Henrique-Silva, F. (2006). *Protein Expr. Purif.* **45**, 324–328.

Rose, S. A., Leek, J. P., Moynihan, T. P., Ardley, H. C., Markham, A. F. & Robinson, P. A. (1998). *Cytogenet. Cell Genet.* **83**, 98–99.

Thompson, J. D., Higgins, D. G. & Gibson, T. J. (1994). *Nucleic Acids Res.* **22**, 4673–4680.

Tiwari, S. & Weissman, A. M. (2001). *J. Biol. Chem.* **276**, 16193–16200.

Vagin, A. & Teplyakov, A. (1997). *J. Appl. Cryst.* **30**, 1022–1025.

Webster, J. M., Tiwari, S., Weissman, A. M. & Wojcikiewicz, R. J. (2003). *J. Biol. Chem.* **278**, 38238–38246.

Yamamoto, M., Kumasaka, T., Ueno, G., Ida, K., Kanda, H., Miyano, M. & Ishikawa, T. (2002). *Acta Cryst.* A**58**, C302.

Yao, M., Zhou, Y. & Tanaka, I. (2006). *Acta Cryst.* D**62**, 189–196.

Zheng, N., Wang, P., Jeffrey, P. D. & Pavletich, N. P. (2000). *Cell*, **102**, 533–539.

Acta Neuropathol (2006) 112:681–689
DOI 10.1007/s00401-006-0132-2

ORIGINAL PAPER

α-Synuclein is colocalized with 14-3-3 and synphilin-1 in A53T transgenic mice

Yoshitomo Shirakashi · Yasuhiro Kawamoto · Hidekazu Tomimoto · Ryosuke Takahashi · Masafumi Ihara

Received: 16 May 2006 / Revised: 6 August 2006 / Accepted: 7 August 2006 / Published online: 7 September 2006

Abstract α-Synuclein is a major constituent of Lewy bodies, the neuropathological hallmark of Parkinson's disease (PD). Three types of α-synuclein mutations, A53T, A30P, and E46K, have been reported in familial PD. Wild-type α-synuclein accumulates at high concentrations in Lewy bodies, and this process is accelerated with mutated A53T α-synuclein. The accumulation of α-synuclein is thought to be toxic, and causes neuronal death when α-synuclein aggregates into protofibrils and fibrils. Lewy bodies contain not only α-synuclein, but also other proteins including 14-3-3 proteins and synphilin-1. 14-3-3 Proteins exist mainly as dimers and are related to intracellular signal transduction pathways. Synphilin-1 is known to interact with α-synuclein, promoting the formation of cytoplasmic inclusions like Lewy bodies in vitro. To investigate the colocalization of α-synuclein, synphilin-1, and 14-3-3 proteins, we performed immunohistochemical studies on α-synuclein, 14-3-3 proteins, and synphilin-1 in the brain and spinal cord of A53T transgenic mice. In homozygous mouse brains, α-synuclein immunoreactivity was observed in the neuronal somata and processes in the medial part of the brainstem, deep cerebellar nuclei, and spinal cord. The distribution of 14-3-3 proteins and synphilin-1 immunoreactivity was similar to that of α-synuclein in the homozygous mice. Double immunofluorescent staining showed that α-synuclein and synphilin-1 or 14-3-3 proteins were colocalized in the pons and spinal cord. These results indicate that the accumulation of mutant α-synuclein occurs in association with 14-3-3 proteins and synphilin-1, and may cause the sequestration of important proteins including 14-3-3 proteins and synphilin-1. The sequestration and subsequent decrease in 14-3-3 proteins and synphilin-1 levels may account for neuronal cell death.

Keywords α-Synuclein · A53T transgenic mice · Parkinson's disease · 14-3-3 Proteins · Synphilin-1 · Immunohistochemistry

Y. Shirakashi (✉) · Y. Kawamoto · H. Tomimoto · R. Takahashi · M. Ihara
Department of Neurology, Graduate School of Medicine, Kyoto University, Sakyo-ku, Kyoto 606-8507, Japan
e-mail: yshiraka@kuhp.kyoto-u.ac.jp

M. Ihara
Biochemistry and Cell Biology Unit, Horizontal Medical Research Organization, Graduate School of Medicine, Kyoto University, Sakyo-ku, Kyoto 606-8507, Japan

Introduction

Parkinson's disease (PD), one of the most common neurodegenerative diseases, is characterized neuropathologically by the presence of intracytoplasmic inclusions called Lewy bodies (LBs), which mainly contain aggregated α-synuclein [34]. Point mutations in the α-*Synuclein* genes have been discovered in families afflicted with autosomal dominant inherited PD [23, 28, 38]. α-Synuclein is expressed predominantly in the presynaptic nerve terminals [13]. Under normal conditions, it is thought to have a role in the modulation of synaptic vesicle turnover and synaptic plasticity [6, 8]. However, this physiological role of α-synuclein is not essential for nerve terminal function, because α-synuclein knockout mice display only a mild phenotype. Nevertheless, α-synuclein is likely to protect nerve terminals under

unusual conditions such as neuronal stress or injuries, since the transgenic expression of α-synuclein has been shown to abolish the lethality and neurodegeneration caused by the deletion of cysteine-string protein-α (CSPα), a co-chaperone protein localized in the synaptic vesicles [6]. Therefore, the loss of functional α-synuclein may predispose dopaminergic neurons to oxidative injury or mitochondrial dysfunction.

Lewy bodies also contain other proteins including ubiquitin [25], parkin [33], cytoskeletal proteins like neurofilaments [32], and septins [16], 14-3-3 proteins [22], and synphilin-1 [36]. The 14-3-3 proteins, a family of protein chaperones, are abundant in the brain, comprising approximately 1% of the total brain proteins [5]. 14-3-3 proteins consist of seven different isoforms, named with Greek letters (β, ε, γ, η, σ, θ, ζ) [12]. 14-3-3 proteins exist mainly as homo- or hetero-dimers consisting of ε and ζ, or θ and ζ subunits, and participate in intracellular signal transduction pathways [1].

14-3-3 Proteins are increased in the cerebrospinal fluid from patients with Creutzfeldt-Jakob disease (CJD), and the detection of 14-3-3 proteins is a marker in the pre-mortem diagnosis of CJD [15]. In recent studies, 14-3-3 proteins were found in abnormal pathological structures, including the neurofibrillary tangles in Alzheimer's disease [24], the Pick bodies in Pick's disease [35], the Lewy bodies in Parkinson's disease [22], the Lewy body-like hyaline inclusions in amyotrophic lateral sclerosis [21], the glial cytoplasmic inclusions in multiple system atrophy [20], the nuclear inclusions in spinocerebellar ataxia-1 [7], the prion plaques in sporadic CJD, and the florid plaques in variant CJD [30]. Ostrerova et al. [27] showed that regions of α-synuclein and 14-3-3 proteins share over 40% homology, and bind to each other. These proteins were found to oppositely regulate parkin activity [31], suggesting important roles for 14-3-3 and α-synuclein together with parkin in the pathogenesis of PD.

On the other hand, Engelender et al. [10] identified synphilin-1, a novel protein which also interacts with α-synuclein to form cytoplasmic inclusions in vitro. The C-terminus of synphilin-1 is closely associated with the C-terminus of α-synuclein [19]. The function of synphilin-1 is not fully understood yet; however, it is enriched in the presynaptic terminals, possibly mediating the synaptic function attributed to α-synuclein [29]. Synphilin-1 is enriched in the central cores of LBs, and is presumed to play a role in LB formation in vivo [36]. Recently, Eyal et al. [11] identified synphilin-1A, an isoform of synphilin-1, which has enhanced aggregatory properties and causes neurotoxicity. Synphilin-1A is also observed in LBs. Synphilin-1 and synphilin-1A differ in their exon organization, and are translated from different start codons. Therefore, the N-terminus of synphilin-1A is different from that of synphilin-1. In addition, a mutation of the synphilin-1 gene has been detected in two German PD patients [26]. Collectively, clarifying the roles of α-synuclein, 14-3-3, and synphilin-1 in the process of LB formation may shed some light on the pathogenesis of PD.

In this study, we examined A53T-Tg mice, which overexpress mutated human A53T α-synuclein under the control of a prion promoter, using immunohistochemistry for α-synuclein, the seven 14-3-3 isoforms, and synphilin-1. α-Synuclein has a tendency to self-aggregate and form fibrils in the presence of the familial PD-linked A53T mutation of α-synuclein [9], and the A53T-Tg mice show numerous α-synuclein-based aggregates in the brain [14]. We determined the distribution of the seven 14-3-3 isoforms and synphilin-1 in the aggregates from these mice to uncover the roles of 14-3-3 proteins and synphilin-1 in the pathogenesis of PD.

Materials and methods

Transgenic mice expressing A53T mutant human α-synuclein (A53T-Tg mice)

We used transgenic mice expressing the A53T mutant human α-synuclein (A53T-Tg mice), which were described in a previous paper [14]. In brief, these Tg mice were generated by using the MoPrP. Xho expression vector, which drives the high expression of A53T mutant human α-synuclein in most CNS neurons. Homozygous A53T-Tg mice develop a motor phenotype, but their litter heterozygous A53T-Tg mice show no neurological symptoms or signs, at least before they become 20 months old. We investigated five homozygous A53T-Tg mice and five heterozygous A53T-Tg mice.

Tissues

The A53T-Tg mice were deeply anesthetized with sodium pentobarbital and then perfused transcardially with 0.01 M phosphate-buffered saline (PBS; Nacalai Tesque, Kyoto, Japan), followed by a fixative containing 4% paraformaldehyde and 0.2% picric acid in 0.1 M phosphate buffer (pH 7.4). Following the surgical removal of the brains and spinal cords, the tissues were fixed for 24 h in the same fixatives, and then stored in 20% sucrose in 0.1 M PBS (pH 7.4). The brains and spinal cords were sliced into coronal and axial sections, respectively (20 μm thick) on a cryostat.

Primary antibodies

As the primary antibodies, we used a goat polyclonal anti-α-synuclein antiserum [C-20; Santa Cruz Biotechnology (SCB), diluted 1:500], a rabbit polyclonal anti-α-synuclein antiserum (C-20R; SCB, diluted 1:500), a rabbit polyclonal anti-human synphilin-1 antiserum (Sy-1-C; an antibody to the C-terminal region of synphilin-1, 1:100) [17], a rabbit polyclonal anti-ubiquitin antiserum (U5379; SIGMA, diluted 1:1,000), and several types of anti-14-3-3 antibodies: a rabbit polyclonal anti-14-3-3β antiserum (C-20; SCB, diluted 1:2,000), a goat polyclonal anti-14-3-3β antiserum (A-15; SCB, diluted 1:1,000), a rabbit polyclonal anti-14-3-3γ antiserum (C-16; SCB, diluted 1:2,000), a rabbit polyclonal anti-14-3-3ζ antiserum (C-16; SCB, diluted 1:2,000), a rabbit polyclonal anti-14-3-3θ antiserum (C-17; SCB, diluted 1:2,000), a rabbit polyclonal anti-14-3-3ε antiserum (T-16; SCB, diluted 1:400), a goat polyclonal anti-14-3-3η antiserum (E-12:SCB, diluted 1:400), a goat polyclonal anti-14-3-3σ antiserum (C-18, against the C-terminus of 14-3-3σ; SCB, diluted 1:400), and a goat polyclonal anti-14-3-3σ antiserum (N-14, against the N-terminus of 14-3-3σ; SCB, diluted 1:400).

Immunohistochemistry

The brain and spinal cord sections were incubated with the primary antibodies in 0.1 M PBS overnight at 4 C. Subsequently, these sections were treated with the appropriate biotinylated secondary antibodies (diluted 1:200; Vector Laboratories, Burlingame, CA, USA) for 1 h at room temperature, followed by an incubation with an avidin–biotin–peroxidase complex (ABC) kit (Vector) diluted in 0.1 M PBS (1:200) for 1 h at room temperature. The sections were visualized with 0.01% diaminobenzidine tetrahydrochloride (DAB; Dojin, Kumamoto, Japan), and 0.005% H_2O_2 in 0.05 M Tris–HCl (pH 7.6) for 10 min at room temperature. Adjoining sections were used for the immunohistochemical investigation of α-synuclein, synphilin-1, and 14-3-3 proteins in the brain and the spinal cord.

Double labeling immunohistochemistry

To investigate the relationship between α-synuclein and 14-3-3 proteins or synphilin-1, the brain sections were incubated with primary antibodies raised against α-synuclein and 14-3-3 or synphilin-1, followed by immunofluorescent staining procedures with fluorescein isothiocyanate-conjugated swine anti-goat immunoglobulins (ACI0408; Biosource) and tetramethylrhodamine-conjugated swine anti-rabbit immunoglobulins (R0156; DAKO).

Results

Distribution of α-synuclein immunoreactivity

In the homozygous mouse brains, α-synuclein immunoreactivity was observed in the neuronal somata and processes. Some α-synuclein immunoreactivity in the somatodendritic compartment appeared as LB-like inclusions. These α-synuclein immunoreactive granules were abundant in the medial part of the midbrain and pons (Figs. 1a, 4), deep cerebellar nuclei (DCN) (Fig. 1b), and spinal cord (Fig. 1c). In these areas, a similar immunolabeling pattern was also observed for ubiquitin (Fig. 1e–g). In age-matched litter heterozygous mouse brains, however, immunostaining for α-synuclein was observed in the neuropil, without any immunostaining in the somatodendritic compartment (Fig. 1d).

Synphilin-1 immunoreactivity

Immunoreactivity for synphilin-1 in the homozygous mice was observed in the somatodendritic compartment of the pons (Fig. 2a), DCN (Fig. 2b) and spinal cord (Fig. 2c). There was no immunoreactivity for synphilin-1 in the axons. In the heterozygous mouse brains, no or faint immunoreactivity for synphilin-1 was detected (Fig. 2d).

14-3-3 Protein immunoreactivity

In the homozygous mice, immunoreactivity for 14-3-3ζ was observed mainly in the somatodendritic compartment in the medial part of the brainstem, motor cortex, and caudoputamen; however, faint immunoreactivity was detected in the spinal cord. 14-3-3ζ immunoreactivity in the heterozygous mice was observed mainly in the cerebral cortex and caudoputamen, but was not detected in the pons (Fig. 2e). Immunoreactivity for 14-3-3β, γ, and θ in the homozygous mouse brains was found mainly in the somatodendritic compartment of the pons, and spinal cord (Fig. 2f, g). In the heterozygous mice, immunoreactivity for 14-3-3β (C-20), γ, and θ was positive in the cerebral cortex, pons, and deep cerebellar nucleus, but there was no or faint immunoreactivity in the spinal cord (Fig. 2h). In the heterozygous mice, immunoreactivity for 14-3-3β (A-15) was also observed in the cerebral cortex, pons, deep cerebellar nucleus, and spinal cord. However, in the

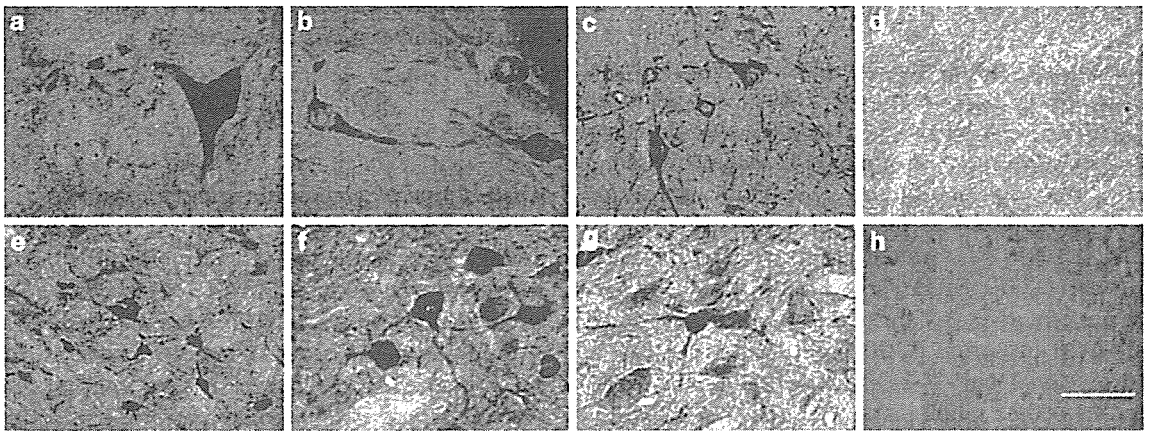

Fig. 1 Immunostaining for α-synuclein (**a–d**) and ubiquitin (**e–h**) in homozygous mice (**a–c, e–g**) and heterozygous mice (**d, h**). The photomicrographs were taken from the pons (**a, e**), deep cerebellar nucleus (**b, f**), and cervical spinal cord (**c, d, g, h**). Strong immunoreactivity for α-synuclein and ubiquitin was observed in the somatodendritic compartment in the pons, deep cerebellar nucleus, and cervical cord in the homozygous mice. In the heterozygous mice, no or faint immunoreactivity was observed in the somatodendritic compartment (**d, h**). *Scale bar* 50 μm (**a–c, f, g**), 100 μm (**d, e, h**)

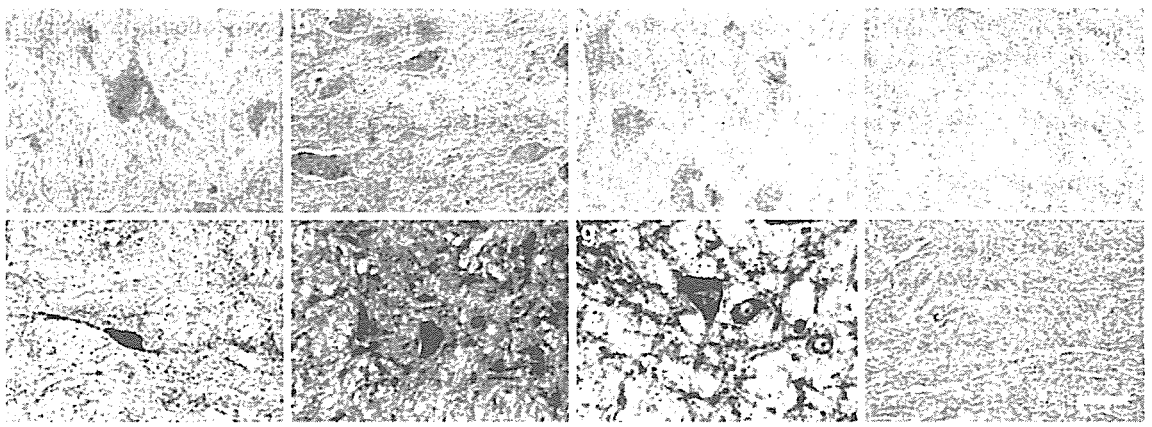

Fig. 2 Immunostaining for synphilin-1 (**a–d**) and 14-3-3 [**e–h**; **e** 14-3-3ζ, **f** 14-3-3β (A-15), **g–h** 14-3-3γ] in homozygous mice (**a–c, e–g**) and heterozygous mice (**d, h**). The photomicrographs were taken from the pons (**a, e**), deep cerebellar nucleus (**b**), lumbar spinal cord (**f**), and cervical spinal cord (**c, d, g, h**). Strong immunoreactivity for synphilin-1, 14-3-3ζ, 14-3-3β, and 14-3-3γ was observed in the somatodendritic compartment in the pons, deep cerebellar nucleus, and spinal cord in the homozygous mice. In the heterozygous mice, no or faint immunoreactivity was observed in the somatodendritic compartment (**d, h**). *Scale bar* 50 μm (**a–c, e–g**), 100 μm (**d, h**)

homozygous mice, strong 14-3-3β (A-15) immunoreactivity was observed in the granules of the neuronal somata and dendrites (Fig. 2f). Immunoreactivity for 14-3-3ε in the homozygous mice was localized to the neuronal nuclei in the cerebral cortex, brainstem, deep cerebellar nuclei, and spinal cord. In the heterozygous mice, 14-3-3ε immunoreactivity was observed also in the same areas as the homozygous mice, except for the spinal cord.

Immunoreactivity for 14-3-3η and σ in the homozygous mice was localized to the neuronal somatodendritic components in the cerebral cortex, brainstem, deep cerebellar nuclei, and spinal cord. Immunoreactivity for 14-3-3η and σ in the heterozygous mice was also observed in the same areas as the homozygous mice, and there were no remarkable differences in the distribution of 14-3-3η and σ between the homozygous and heterozygous mice.

Double immunofluorescent staining

In the homozygous mice, the distribution of immunoreactivity for synphilin-1 and 14-3-3 was mainly observed in the medial part of the midbrain and pons, DCN, and spinal cord, and was similar to that of α-synuclein (Fig. 4).

Double-immunofluorescent-stained sections in the homozygous mice showed that 14-3-3β and γ were colocalized with α-synuclein in the spinal cord. 14-3-3ζ was colocalized with α-synuclein in the pons. Synphilin-1 was also colocalized with α-synuclein in the pons (Fig. 3). By randomly sampling three arbitrary regions in the pons, the mean frequencies of double labeling for 14-3-3β, γ, θ, ζ, and ε immunoreactivities with α-synuclein were 83, 70, 66, 44, and 56%, respectively, in the homozygous mice.

Discussion

The most notable finding of this study using the A53T-Tg mice was that α-synuclein overexpression alone was enough to induce aggregates containing α-synuclein, 14-3-3 proteins, and synphilin-1, which are partially reminiscent of LBs. Given the fact that the difference between homozygous and heterozygous A53T-Tg mice is limited to the magnitude of expression of the transgene-derived human α-synuclein, and that the expres-

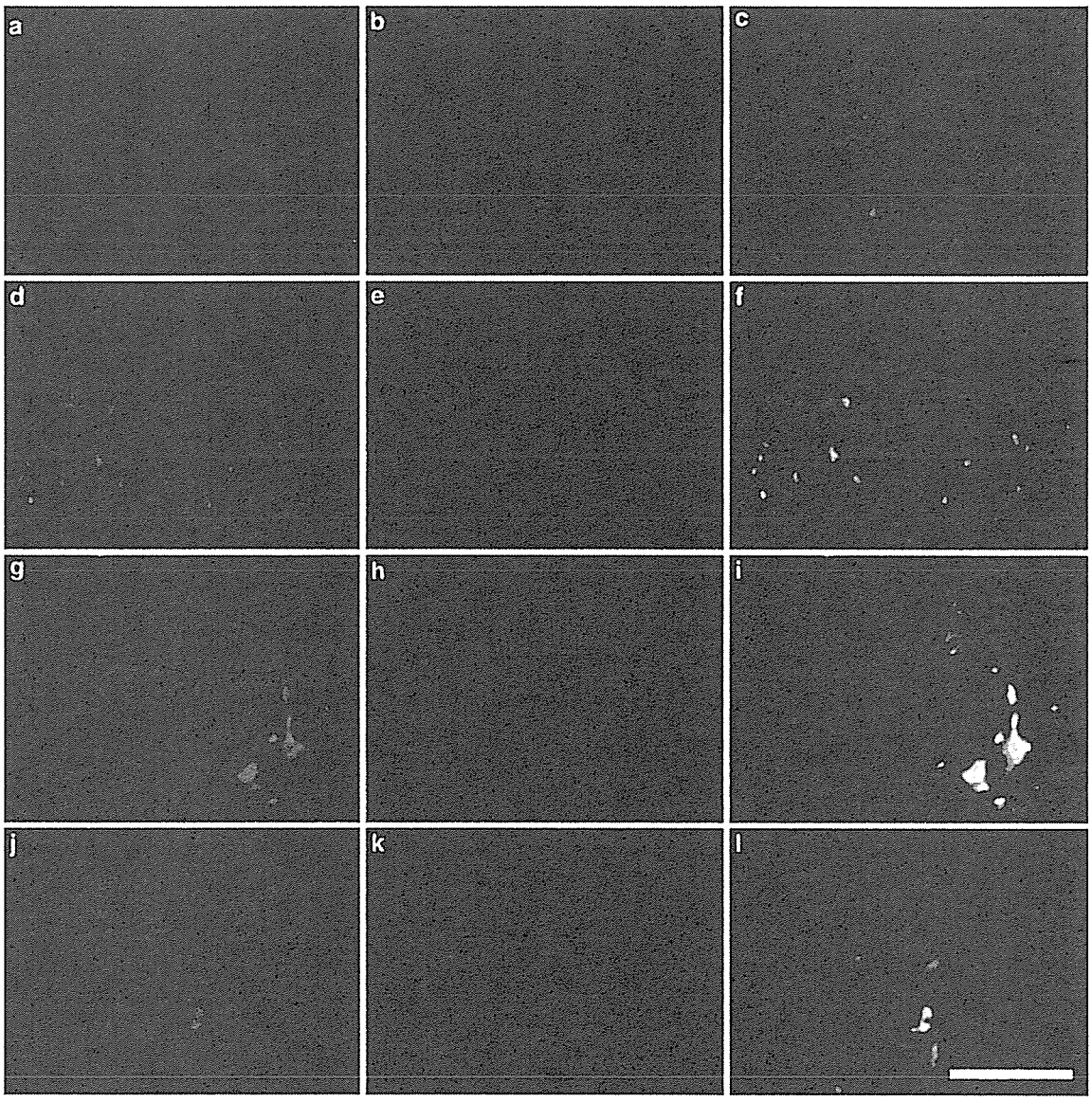

Fig. 3 Double immunofluorescent staining for α-synuclein plus synphilin-1 (**a–c**), and α-synuclein plus 14-3-3 (**d-l**) in homozygous mice. **a–f** pons; **g–i** lumbar spinal cord; and **j–l** thoracic spinal cord. The *left column* (**a**, **d**, **g**, **j**; *green*) shows immunostaining for α-synuclein, and the *middle column* shows (**b**, **e**, **h**, **k**; *red*) immunostaining for synphilin-1 (**b**), 14-3-3ζ (**e**), 14-3-3γ (**h**), and 14-3-3β (**k**). The *right column* (**c**, **f**, **i**, **l**) shows the merged image. *Scale bar* 50 μm (**a–c**), 100 μm (**d–l**)

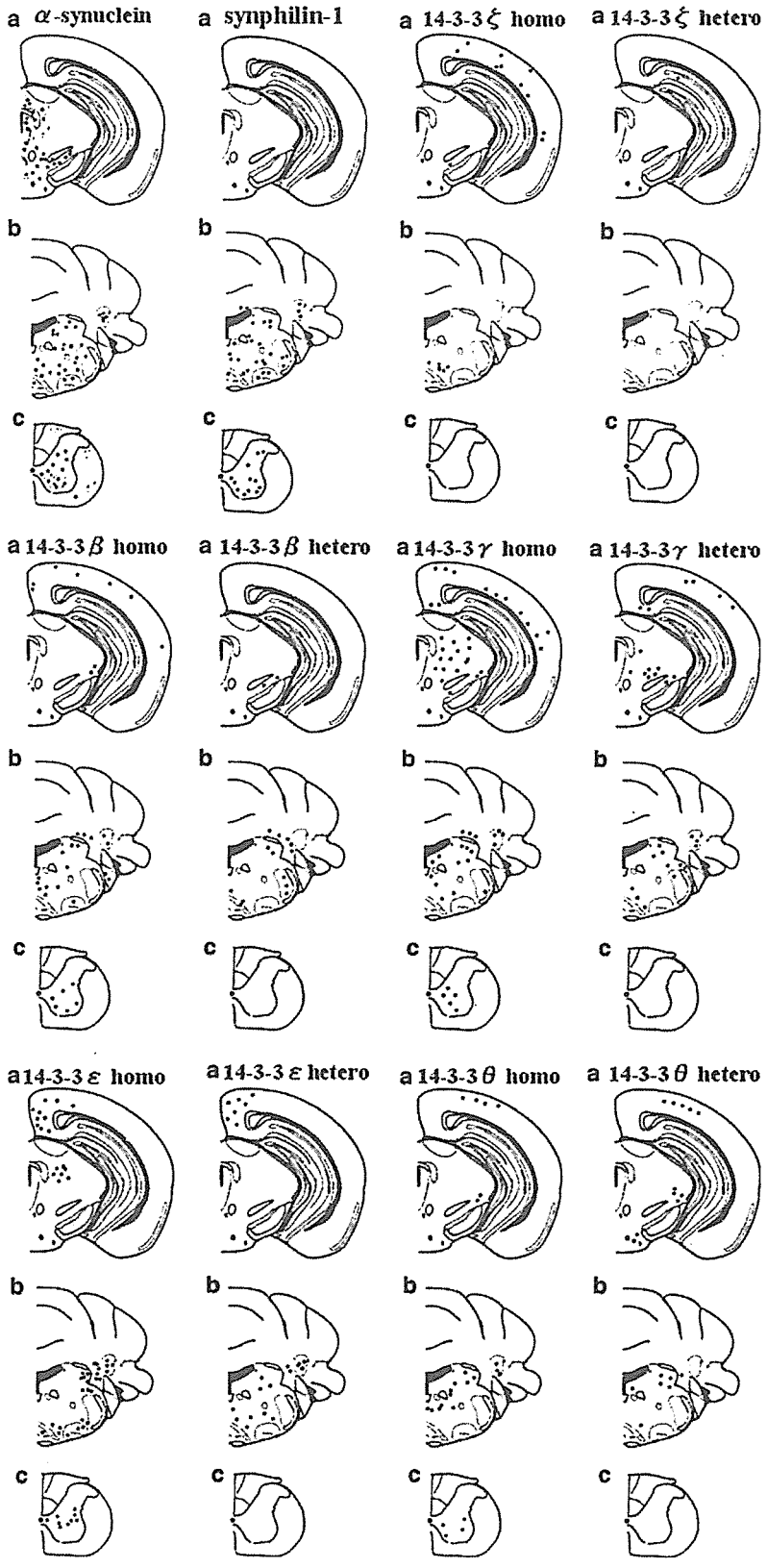

Fig. 4 Schematic distribution of α-synuclein (*α-syn*), synphilin-1 (*sph*), and 14-3-3 in A53T-Tg mice. A schematic summary of the α-synuclein, synphilin-1, and 14-3-3 pathology was shown as coronal sections from the A53T-Tg mouse brain and spinal cord, at the level of the midbrain (**a**), pons and deep cerebellar nucleus (**b**), and the cervical spinal cord (**c**). The *dots* represent one to three neurons with immunoreactivity for each antigen

sion level is approximately 20× higher than the endogenous expression observed in homozygous A53T-Tg mice [14], 14-3-3 proteins and synphilin-1 are more likely to be sequestered into the aggregates, rather than stoichiometrically associated with α-synuclein to form insoluble complexes. The sequestration of 14-3-3 proteins and synphilin-1 into aggregates may decrease the amount of functional 14-3-3 proteins and synphilin-1 available in the synaptic terminal, possibly disrupting chaperone and synaptic functions, respectively.

Under normal conditions, α-synuclein exists as a relatively unfolded molecule in the presynaptic terminals. However, under pathological conditions, it forms fibrils, accumulates in the neuronal somata, and may form inclusion bodies. In the heterozygous mice, α-synuclein has been reported to exhibit a neuropil immunostaining pattern [14], and this study showed a similar result without any immunoreactivities for α-synuclein in the somatodendritic compartment. Immunoreactivities for 14-3-3β and γ in the normal mouse brain have been localized to neurons in the brainstem and cerebral cortex, but not in the spinal cord [3]. These immunostaining patterns were similar in the heterozygous mice, in which the neuronal immunolabeling for 14-3-3β and γ occurred in the brainstem and cerebral cortex. In contrast, in the homozygous mice, 14-3-3γ accumulated in the spinal anterior horn cells (Fig. 4).

The immunostaining patterns for 14-3-3β in the homozygous mice have been strongly positive in the granules from the neuronal somata and dendrites in the spinal cord. The homozygous mice have been shown to develop motor impairments, possibly due to a degeneration of the anterior horn cells. Therefore, this accumulation of 14-3-3β and γ in the anterior horn cell bodies may play a significant role in the development of motor symptoms in these mice. Previously, we showed that LB-like hyaline inclusions in the anterior horn cells were immunoreactive for several 14-3-3 proteins in patients with amyotrophic lateral sclerosis [21]. Taken together, the accumulation of 14-3-3 proteins in the somatodendritic compartments of the anterior horn cells may be generally associated with a dysfunction of the lower motor neurons.

Synphilin-1A, an isoform of synphilin-1, is localized to the LBs and is an aggregation-prone protein that causes neuronal toxicity [11]. In this study, we used an anti-synphilin-1 antibody which recognizes the C-terminus of synphilin-1, and thus there was the possibility that this anti-synphilin-1 antibody may have cross-reacted, and showed the localization of synphilin-1A in the homozygous mice. Increasing evidence further supplements the conjugation of α-synuclein with 14-3-3 proteins or synphilin-1. In cell cultures, the co-transfection of synphilin-1 and α-synuclein has been shown to promote the formation of eosinophilic cytoplasmic inclusions like LBs [10]. Xu and colleagues [37] showed that soluble wild-type and mutant α-synuclein form complexes with 14-3-3 proteins, and accumulate in dopaminergic neurons. The colocalization of 14-3-3 proteins or synphilin-1 with α-synuclein in LBs has been demonstrated in human brains [22, 36]. Under non-pathological conditions, 14-3-3 proteins inhibit apoptosis by binding and inactivating pro-apoptotic proteins, including the mitochondrial Bcl-2 family member BAD and the transcription factor Forkhead [39]. Berg et al. [4] showed that 14-3-3 proteins, especially the ε, γ, θ, and ζ isoforms, were colocalized in the LBs. Kaneko and Hachiya [18] proposed the possibility that the distinctive function of 14-3-3ζ might be a sweeper of misfolded proteins such as aggregates or inclusion bodies. In our study, enhanced immunoreactivity for 14-3-3 proteins and synphilin-1 was observed in the A53T-Tg homozygous mice. According to these results, the 14-3-3 proteins bound to the overexpressed α-synuclein, and thus forming complexes of these proteins which may lead to the sequestration and subsequent decrease in 14-3-3 proteins. In turn, this decrease in 14-3-3 proteins causes the apoptotic neuronal cell death. Furthermore, those 14-3-3 proteins which interact with α-synuclein and accumulate in LBs may also interact with synphilin-1 [2]. The sequestration of synphilin-1 may also contribute to neuronal dysfunction, possibly through an impairment of synaptic function attributed to α-synuclein, although the exact role of synphilin-1 remains to be fully understood. The present study showed that α-synuclein colocalized with 14-3-3 proteins and synphilin-1, suggesting that these multi-protein complexes formed by α-synuclein, synphilin-1, and 14-3-3 proteins may account for the pathogenesis of neuronal cell death.

Acknowledgments We are grateful to Prof. V. M. Lee (Department of Pathology and Laboratory Medicine, University of Pennsylvania) for providing the A53T-Tg mice, and to Prof. E. Iseki (Department of Psychiatry, Juntendo University School of Medicine) for providing the anti-synphilin-1 antibodies.

References

1. Aitken A (1996) 14-3-3 and its possible role in co-ordinating multiple signalling pathways. Trends Cell Biol 6:341–347
2. Avraham E, Szargel R, Eyal A, Rott R, Engelender S (2005) Glycogen synthase kinase 3beta modulates synphilin-1 ubiquitylation and cellular inclusion formation by SIAH: implications for proteasomal function and Lewy body formation. J Biol Chem 280:42877–42886

3. Baxter HC, Liu WG, Forster JL, Aitken A, Fraser JR (2002) Immunolocalisation of 14-3-3 isoforms in normal and scrapie-infected murine brain. Neuroscience 109:5–14
4. Berg D, Riess O, Bornemann A (2003) Specification of 14-3-3 proteins in Lewy bodies. Ann Neurol 54:135
5. Boston PF, Jackson P, Thompson RJ (1982) Human 14-3-3 protein: radioimmunoassay, tissue distribution, and cerebrospinal fluid levels in patients with neurological disorders. J Neurochem 38:1475–1482
6. Chandra S, Gallardo G, Fernandez-Chacon R, Schluter OM, Sudhof TC (2005) Alpha-synuclein cooperates with CSPalpha in preventing neurodegeneration. Cell 123:383–396
7. Chen HK, Fernandez-Funez P, Acevedo SF, Lam YC, Kaytor MD, Fernandez MH, Aitken A, Skoulakis EM, Orr HT, Botas J, Zoghbi HY (2003) Interaction of Akt-phosphorylated ataxin-1 with 14-3-3 mediates neurodegeneration in spinocerebellar ataxia type 1. Cell 113:457–468
8. Clayton DF, George JM (1999) Synucleins in synaptic plasticity and neurodegenerative disorders. J Neurosci Res 58:120–129
9. Conway KA, Harper JD, Lansbury PT (1998) Accelerated in vitro fibril formation by a mutant alpha-synuclein linked to early-onset Parkinson disease. Nat Med 4:1318–1320
10. Engelender S, Kaminsky Z, Guo X, Sharp AH, Amaravi RK, Kleiderlein JJ, Margolis RL, Troncoso JC, Lanahan AA, Worley PF, Dawson VL, Dawson TM, Ross CA (1999) Synphilin-1 associates with alpha-synuclein and promotes the formation of cytosolic inclusions. Nat Genet 22:110–114
11. Eyal A, Szargel R, Avraham E, Liani E, Haskin J, Rott R, Engelender S (2006) Synphilin-1A: an aggregation-prone isoform of synphilin-1 that causes neuronal death and is present in aggregates from alpha-synucleinopathy patients. Proc Natl Acad Sci USA 103:5917–5922
12. Fu H, Subramanian RR, Masters SC (2000) 14-3-3 proteins: structure, function, and regulation. Annu Rev Pharmacol Toxicol 40:617–647
13. George JM, Jin H, Woods WS, Clayton DF (1995) Characterization of a novel protein regulated during the critical period for song learning in the zebra finch. Neuron 15:361–372
14. Giasson BI, Duda JE, Quinn SM, Zhang B, Trojanowski JQ, Lee VM (2002) Neuronal alpha-synucleinopathy with severe movement disorder in mice expressing A53T human alpha-synuclein. Neuron 34:521–533
15. Hsich G, Kenney K, Gibbs CJ, Lee KH, Harrington MG (1996) The 14-3-3 brain protein in cerebrospinal fluid as a marker for transmissible spongiform encephalopathies. N Engl J Med 335:924–930
16. Ihara M, Tomimoto H, Kitayama H, Morioka Y, Akiguchi I, Shibasaki H, Noda M, Kinoshita M (2003) Association of the cytoskeletal GTP-binding protein Sept4/H5 with cytoplasmic inclusions found in Parkinson's disease and other synucleinopathies. J Biol Chem 278:24095–24102
17. Iseki E, Takayama N, Furukawa Y, Marui W, Nakai T, Miura S, Ueda K, Kosaka K (2002) Immunohistochemical study of synphilin-1 in brains of patients with dementia with Lewy bodies - synphilin-1 is non-specifically implicated in the formation of different neuronal cytoskeletal inclusions. Neurosci Lett 326:211–215
18. Kaneko K, Hachiya NS (2006) The alternative role of 14-3-3 zeta as a sweeper of misfolded proteins in disease conditions. Med Hypotheses 67:169–171
19. Kawamata H, McLean PJ, Sharma N, Hyman BT (2001) Interaction of alpha-synuclein and synphilin-1: effect of Parkinson's disease-associated mutations. J Neurochem 77:929–934
20. Kawamoto Y, Akiguchi I, Nakamura S, Budka H (2002) Accumulation of 14-3-3 proteins in glial cytoplasmic inclusions in multiple system atrophy. Ann Neurol 52:722–731
21. Kawamoto Y, Akiguchi I, Nakamura S, Budka H (2004) 14-3-3 proteins in Lewy body-like hyaline inclusions in patients with sporadic amyotrophic lateral sclerosis. Acta Neuropathol (Berl) 108:531–537
22. Kawamoto Y, Akiguchi I, Nakamura S, Honjyo Y, Shibasaki H, Budka H (2002) 14-3-3 proteins in Lewy bodies in Parkinson disease and diffuse Lewy body disease brains. J Neuropathol Exp Neurol 61:245–253
23. Kruger R, Kuhn W, Muller T, Woitalla D, Graeber M, Kosel S, Przuntek H, Epplen JT, Schols L, Riess O (1998) Ala30Pro mutation in the gene encoding alpha-synuclein in Parkinson's disease. Nat Genet 18:106–108
24. Layfield R, Fergusson J, Aitken A, Lowe J, Landon M, Mayer RJ (1996) Neurofibrillary tangles of Alzheimer's disease brains contain 14-3-3 proteins. Neurosci Lett 209:57–60
25. Lowe J, Blanchard A, Morrell K, Lennox G, Reynolds L, Billett M, Landon M, Mayer RJ (1988) Ubiquitin is a common factor in intermediate filament inclusion bodies of diverse type in man, including those of Parkinson's disease, Pick's disease, and Alzheimer's disease, as well as Rosenthal fibres in cerebellar astrocytomas, cytoplasmic bodies in muscle, and mallory bodies in alcoholic liver disease. J Pathol 155:9–15
26. Marx FP, Holzmann C, Strauss KM, Li L, Eberhardt O, Gerhardt E, Cookson MR, Hernandez D, Farrer MJ, Kachergus J, Engelender S, Ross CA, Berger K, Schols L, Schulz JB, Riess O, Kruger R (2003) Identification and functional characterization of a novel R621C mutation in the synphilin-1 gene in Parkinson's disease. Hum Mol Genet 12:1223–1231
27. Ostrerova N, Petrucelli L, Farrer M, Mehta N, Choi P, Hardy J, Wolozin B (1999) alpha-Synuclein shares physical and functional homology with 14-3-3 proteins. J Neurosci 19:5782–5791
28. Polymeropoulos MH, Lavedan C, Leroy E, Ide SE, Dehejia A, Dutra A, Pike B, Root H, Rubenstein J, Boyer R, Stenroos ES, Chandrasekharappa S, Athanassiadou A, Papapetropoulos T, Johnson WG, Lazzarini AM, Duvoisin RC, Di Iorio G, Golbe LI, Nussbaum RL (1997) Mutation in the alpha-synuclein gene identified in families with Parkinson's disease. Science 276:2045–2047
29. Ribeiro CS, Carneiro K, Ross CA, Menezes JR, Engelender S (2002) Synphilin-1 is developmentally localized to synaptic terminals, and its association with synaptic vesicles is modulated by alpha-synuclein. J Biol Chem 277:23927–23933
30. Richard M, Biacabe AG, Streichenberger N, Ironside JW, Mohr M, Kopp N, Perret-Liaudet A (2003) Immunohistochemical localization of 14.3.3 zeta protein in amyloid plaques in human spongiform encephalopathies. Acta Neuropathol (Berl) 105:296–302
31. Sato S, Chiba T, Sakata E, Kato K, Mizuno Y, Hattori N, Tanaka K (2006) 14-3-3eta is a novel regulator of parkin ubiquitin ligase. Embo J 25:211–221
32. Schmidt ML, Murray J, Lee VM, Hill WD, Wertkin A, Trojanowski JQ (1991) Epitope map of neurofilament protein domains in cortical and peripheral nervous system Lewy bodies. Am J Pathol 139:53–65
33. Shimura H, Schlossmacher MG, Hattori N, Frosch MP, Trockenbacher A, Schneider R, Mizuno Y, Kosik KS, Selkoe DJ (2001) Ubiquitination of a new form of alpha-synuclein by parkin from human brain: implications for Parkinson's disease. Science 293:263–269
34. Spillantini MG, Schmidt ML, Lee VM, Trojanowski JQ, Jakes R, Goedert M (1997) Alpha-synuclein in Lewy bodies. Nature 388:839–840

35. Umahara T, Uchihara T, Tsuchiya K, Nakamura A, Ikeda K, Iwamoto T, Takasaki M (2004) Immunolocalization of 14-3-3 isoforms in brains with Pick body disease. Neurosci Lett 371:215–219
36. Wakabayashi K, Engelender S, Yoshimoto M, Tsuji S, Ross CA, Takahashi H (2000) Synphilin-1 is present in Lewy bodies in Parkinson's disease. Ann Neurol 47:521–523
37. Xu J, Kao SY, Lee FJ, Song W, Jin LW, Yankner BA (2002) Dopamine-dependent neurotoxicity of alpha-synuclein: a mechanism for selective neurodegeneration in Parkinson disease. Nat Med 8:600–606
38. Zarranz JJ, Alegre J, Gomez-Esteban JC, Lezcano E, Ros R, Ampuero I, Vidal L, Hoenicka J, Rodriguez O, Atares B, Llorens V, Gomez Tortosa E, del Ser T, Munoz DG, de Yebenes JG (2004) The new mutation, E46K, of alpha-synuclein causes Parkinson and Lewy body dementia. Ann Neurol 55:164–173
39. Zha J, Harada H, Yang E, Jockel J, Korsmeyer SJ (1996) Serine phosphorylation of death agonist BAD in response to survival factor results in binding to 14-3-3 not BCL-X(L). Cell 87:619–628

Matrix Metalloproteinase-2 Plays a Critical Role in the Pathogenesis of White Matter Lesions After Chronic Cerebral Hypoperfusion in Rodents

Kayoko Nakaji, MD; Masafumi Ihara, MD; Chiaki Takahashi, MD; Shigeyoshi Itohara, PhD; Makoto Noda, PhD; Ryosuke Takahashi, MD; Hidekazu Tomimoto, MD

Background and Purpose—Cerebrovascular white matter (WM) lesions contribute to cognitive impairment and motor dysfunction in the elderly. A disruption of the blood–brain barrier (BBB) is believed to be a critical early event leading to these WM lesions. Previous studies have suggested the involvement of matrix metalloproteinase-2 (MMP-2) in BBB disruptions and the upregulation of MMP-2 after chronic cerebral hypoperfusion in a rat model. In the present study, we asked whether MMP-2 is involved in the BBB disruption and the subsequent WM lesions after chronic cerebral hypoperfusion.

Methods—We compared the severity of white matter lesions in rats after chronic cerebral hypoperfusion with or without an MMP inhibitor. Then, we also induced the chronic cerebral hypoperfusion in wild-type and MMP-2-null mice.

Results—In the rats treated with a relatively selective MMP-2 inhibitor, AG3340, the WM lesions after chronic cerebral hypoperfusion were significantly less severe, and the number of activated astroglia and microglia were also significantly lower as compared with the vehicle-treated rats. Gene knockout of MMP-2 also reduced the severity of the WM lesions and the number of activated astroglia and microglia in a mice system. In both rodents, the disruption of BBB function, as assessed by IgM staining and the Evans blue extravasation test, was less severe when MMP-2 activity was attenuated.

Conclusions—These findings indicate that MMP-2 plays a critical role in the BBB disruption, glial cell activation, and WM lesions after chronic cerebral hypoperfusion and suggest the potential value of MMP-2 inhibitors as a therapeutic tool in cerebrovascular WM lesions. (***Stroke*. 2006;37:2816-2823.)**

Key Words: blood–brain barrier ■ chronic cerebral hypoperfusion ■ MMP inhibitor ■ MMP-2 ■ white matter lesion

Cerebrovascular white matter (WM) lesions, a neurodegenerative condition characterized by hyperintense signals on magnetic resonance images, are frequently associated with aging and cerebrovascular disease and are responsible for the cognitive decline of the elderly. Chronic cerebral ischemia is likely to cause these WM lesions, because cerebral blood flow is decreased in these patients.[1] Indeed, similar WM lesions can be induced in rats and mice after chronic cerebral hypoperfusion, the experimental conditions mimicking chronic cerebral ischemia in humans.[2,3]

Matrix metalloproteinases (MMPs) are a family of endopeptidases that can degrade most of the major constituents of the extracellular matrix.[4] MMP-2 and MMP-9 represent a subgroup of the MMP family and degrade several extracellular matrix components, including type IV collagen, fibronectin, and gelatin. Deregulated MMPs have been implicated in the tissue destruction associated with cancer, arthritis, and multiple sclerosis.[4] MMPs may also play a role in neurologic disorders. For instance, MMP-9 is increased in human brains after stroke,[5] and MMP-2 and MMP-3 are increased in cerebrovascular WM lesions from patients with vascular dementia.[6] A reduction in the basement membrane components, including type IV collagen, is associated with the blood–brain barrier (BBB) disruption during cerebral ischemia.[7] In our previous study on chronic cerebral hypoperfusion, the BBB disruption was accompanied by an upregulation of MMP-2 but not MMP-9,[8] suggesting the specific involvement of MMP-2 in the WM lesions. We hypothesize that the MMP-2 upregulation after chronic cerebral hypoperfusion correlates with BBB damage, which leads to glial activation and subsequent WM lesions. To clarify the cause–effect relationship among MMP-2 upregulation, BBB disruption, and WM lesions, we used 2 strategies to attenuate MMP-2 activity: an MMP inhibitor, AG3340, and MMP-2

Received March 2, 2006; final revision received June 9, 2006; accepted July 24, 2006.

From the Department of Neurology (K.N., M.I., R.T., H.T.), Horizontal Medical Research Organization (M.I.), the Department of Molecular Oncology (M.N.), and The 21st Century Center of Excellence Program, Department of Oncology (C.T.), Kyoto University Graduate School of Medicine, Kyoto, Japan; and the Laboratory for Behavioral Genetics (S.I.), RIKEN Brain Science Institute, Wako, Japan.

Correspondence to Kayoko Nakaji, MD, Department of Neurology, Graduate School of Medicine, Kyoto University, 54 Kawaharamachi, Shogoin, Sakyo-ku, Kyoto 606-8507, Japan. E-mail kann@kuhp.kyoto-u.ac.jp

Stroke **is available at http://www.strokeaha.org** **DOI: 10.1161/01.STR.0000244808.17972.55**

knockout. The results from both experiments strongly supported the idea that MMP-2 plays a critical role in BBB disruption and WM lesions.

Materials and Methods

Chronic Cerebral Hypoperfusion in Rats and Treatment With an Matrix Metalloproteinase Inhibitor

Chronic cerebral hypoperfusion with bilateral common carotid artery occlusion (BCAO) was induced in male Wistar rats (weight 150 to 200 g; Shimizu Experimental Supply; Kyoto, Japan) by double ligation of the common carotid arteries as previously described.[2] After the operation, the rats were kept in animal quarters with food and water ad libitum.

AG3340 (Agouron Pharmaceuticals) was dissolved at 75 mg/mL in 50% DMSO in propylenglycol. The rats were treated twice a day with an intraperitoneal injection of AG3340 (100 mg/kg) or vehicle (DMSO/propylenglycol) from just before the operation until 14 days after the operation. Similar doses and treatment paradigms have been shown to be effective in inhibiting MMP activity in gliomas in model animals.[9] Because our previous study demonstrated that the number of microglia peaked on 3 days and WM lesion started to become evident on 14 days after BCAO,[2] the animals were subjected to the analyses described subsequently.

Mice

The generation of C57BL/6J mice carrying the MMP-2-null allele has been described elsewhere.[10] In this mutant allele, a region containing the promoter and the first exon of the MMP-2 gene is replaced by the pgk-neo cassette. MMP-$2^{\pm}$ parents were mated to obtain both wild-type and MMP-$2^{-/-}$ (MMP-2-null) littermates. Genotyping was performed by polymerase chain reaction using the following primers: wild-type forward, CAACGATGGAGGCACGAGTG; wild-type reverse, GCCGGGGAACTTGATGATGG; mutant forward, CTTGGGTGGAGAGGCTATTC; and mutant reverse, AGGTGAGATGACAGGAGATC.

Chronic Cerebral Hypoperfusion in Mice and Cerebral Blood Flow Measurement

Adult male mice (weight 20 to 25 g) were subjected to bilateral common carotid arteries stenosis (BCAS) by applying the microcoils with an inner diameter of 0.18 mm to both common carotid arteries as previously described.[3] The cerebral blood flow (CBF) was recorded by laser Doppler flowmetry by placing a straight probe (OmegaFLO-N1; Neuroscience Inc) on 1 mm posterior and 2 mm lateral from bregma perpendicular to the skull bone through the guide cannula. The baseline CBF recordings were obtained just before and at 2 hours and 3, 7, 14, and 30 days after the surgery. The CBF values were expressed as a percentage of the baseline value.

Histochemical Evaluation of White Matter Lesions and Glial Activation

Under deep anesthesia, the animals were perfused with 10 mmol/L phosphate-buffered saline (300 mL for rats, 100 mL for mice) and then with a fixative consisting of 4% paraformaldehyde, 0.2% picric acid, and 0.1 mol/L phosphate buffer at pH 7.4 (300 mL for rats, 100 mL for mice). The brains were removed and postfixed for 24 hours in 4% paraformaldehyde in 0.1 mol/L phosphate buffer and then stored in 15% sucrose in 0.1 mol/L phosphate buffer. The fixed brains were embedded in paraffin and sliced into 2-μm-thick coronal sections. Klüver-Barrera staining and Bielschowsky staining were used to visualize the myelin sheaths and axons, respectively. As previously described,[2] the severity of the WM lesions was semiquantitatively graded as normal (grade 0), disarrangement of the nerve fibers (grade 1), formation of marked vacuoles (grade 2), and disappearance of myelinated fibers (grade 3) by an investigator blind to the experimental condition. For immunohistochemistry, serial sections (20-μm-thick) were cut in a cryostat and incubated overnight with a primary antibody at 4°C followed by incubation with the appropriate biotinylated secondary antibody (1 hour, room temperature), treatment with an avidin–biotin complex (diluted 1:200; Vector Laboratories), and visualization with 0.01% diaminobenzidine tetrahydrochloride and 0.005% H_2O_2 in 50 mmol/L Tris-HCl (pH 7.6). The primary antibodies used were as follows: monoclonal anti-rat glial fibrillary acidic protein (GFAP) (diluted 1:5000; Sigma-Aldrich; Mo, USA), polyclonal rabbit anti-mouse GFAP (diluted to 1:5000; Dako Cytomation, Denmark), polyclonal rabbit anti-MMP-2 (diluted to 1: 1,000, Chemicon International, Inc), monoclonal rat anti-mouse MHC class II antigen antibodies (diluted to 1:5000; Dako Cytomation), and rabbit anti Iba-1 antibody (1 μg/mL; Wako Pure Chemical Industries, Ltd; Osaka, Japan). Some sections were incubated with a biotinylated goat anti-rat IgM (μ), biotinylated goat anti-mouse IgM (μ) (diluted 1:1000; Kirkegaad & Perry Laboratories; Md, USA), or biotinylated Ricinus communis agglutinin-1 (diluted 1:1000; Vector Laboratories; Calif, USA) and were incubated directly with the avidin–biotin complex. To confirm the cellular source of IgM, sections were labeled by biotinylated anti-mouse IgM and rabbit anti-mouse GFAP followed by fluorescein isothiocyanate-labeled avidin (diluted 1:100; Dako Cytomation) and rhodamine-labeled goat anti- rabbit IgG (2.5 μL/mL; Dako). In the sections immunostained for Ricinus communis agglutinin-1, MHC class II antigen, Iba-1, GFAP, and IgM, we counted the number of immunopositive cells in at least 6 representative fields (per 0.25 mm^2) in the corpus callosum, the caudoputamen, and the optic tract for the quantitative analysis.

Zymography and Matrix Metalloproteinases-2 Activity Assay

Minced forebrain tissues were incubated with gentle rotation at 4°C for 20 hour in an extraction buffer consisting of 0.5% Triton-X 100, 0.5 U/mL aprotinin, and 0.01% sodium azide in 0.01 mol/L phosphate-buffered saline. The samples were then centrifuged at 14 000 rpm for 15 minutes at 4°C and the supernatants were collected. The protein content was adjusted to 10 mg/mL. The gelatinolytic activity of these samples was detected by SDS-PAGE zymography as described elsewhere,[8] although MMP-2 activity in the gray matter may interfere a sensitive detection of the activity in the WM. Equal amounts of tissue extract (50 μg) were then subjected to electrophoresis. To restore the activity of the protein, sample gels were agitated in 0.01 mol/L Tris-HCl (pH 8.0) containing 2.5% Triton X-100 (30 minutes×2). After washed in 0.05 mol/L Tris-HCl (pH 8.0) for 30 minutes, the gels were incubated overnight twice at 37°C in 0.05 mol/L Tris-HCl (pH 8.0) containing 0.5 mmol/L $CaCl_2$ and 1.0 mol/L $ZnCl_2$. After incubation, the gels were stained with Coomassie blue R-250. The amount of activated and latent forms of MMP-2 in the whole forebrain extracts were also assessed using the Matrix Metalloproteinase-2 Biotrak Activity Assay System (Amersham Biosciences), which is based on a 2-site enzyme-linked immunosorbent assay "sandwich" format and recognizes both the proform and active form of MMP-2.

Evans Blue Extravasation

The mice were killed at 3 hours and 1, 3, 5, 7, and 14 days after BCAS. One hour before each time point, 1 mL of 4% Evans blue (EB; Nakalai Chemicals Ltd) in normal saline was injected intraperitoneally. The animals were anesthetized and then perfused transcardially with 200 mL of 10 mmol/L phosphate-buffered saline. The brains were snap-frozen, sectioned into 20-μm-thick slices, and examined by fluorescence microscopy. For quantitative measures, the images were analyzed within 4 structurally similar areas (2 paramedian portions of the corpus callosum on each hemisphere) in each mouse and digitally level-adjusted by Adobe Photoshop (Adobe Systems) so that intravascular EB would be reported as white (pixel value 255) on a black background (pixel value 0). Using the public domain NIH Image 1.61 program (National Institutes of Health), the images were then binarized with intensity threshold set at pixel value 50 so that the white pixels represent intravascular and extravasated EB. The number of white pixels was divided by the total pixel

number in the selected area to estimate percent area containing intravascular and extravasated EB as an approximate index of BBB breakdown. Image analysis was focused on the paramedian portion of the corpus callosum facing the dorsal part of the lateral ventricle, because WM lesions were most intense in this region.[3]

Statistical Analysis

All data are presented as means±SE. A one-factor ANOVA followed by Fisher protected least significant difference procedure was used to compare the differences between groups. P values <0.05 were considered to be statistically significant.

Results

The amount of total MMP-2 in the forebrain extracts was comparable between the vehicle-treated and AG3340-injected rats after BCAO as assessed using the Biotrak Activity Assay System. The percentage of activated MMP-2 was only 7% on day 3 after the sham operation but was elevated to approximately 80% on day 3 after the BCAO (supplemental Figure I, available online at http://stroke.ahajournals.org). We also confirmed almost complete suppression of MMP-2 activation with AG3340 administration.

The operation was successful in rats (n=40) except 3, which developed convulsions and was killed within 7 days, and in mice (n=62) except 4, which developed cerebral infarction. These animals with unsuccessful operations were excluded from the statistical analysis. In the vehicle-treated animals, severe WM lesions, as shown by an increased number of disarranged nerve fibers and vacuolation, were found on day 14 after the BCAO in the optic nerve, medial part of the corpus callosum (Figure 1B and 1E), the internal capsule, and the fiber bundles of the caudoputamen. In such WM regions, the number of Ricinus communis agglutinin-1-positive microglia and GFAP-positive astroglia increased (2- to 3-fold) on day 3 after the BCAO (Figure 1H and 1K). Both WM lesions and gliosis were less severe in the AG3340-treated animals (Figure 1C, 1F, 1I, 1L, 1P through 1R, and Table 1).

The BBB integrity in rats subjected to BCAO was also assessed by the immunostaining for IgM. IgM-immunoreactive glial cells represent those cells that have taken up the serum proteins, which leaked into the brain parenchyma, and their number serves as an indicator of BBB dysfunction.[8] Some IgM-immunoreactive glial cells were found in the vicinity of the microvessels in the corpus callosum in the vehicle-treated animals on day 3 after the BCAO (Figure 1R), suggesting BBB dysfunction in this region. In contrast, much fewer IgM-immunoreactive glia were found in the same area of the AG3340-treated animals (Figure 1O and 1R).

These results strengthen the notion that MMPs play a role in BBB impairment and WM lesions. To further elucidate the roles of MMPs in the WM damage after chronic cerebral hypoperfusion, we applied BCAS (the established technique for mice hypoperfusion)[3] for mice lacking functional MMP-2 gene (MMP-2-null mice), which showed no obvious developmental abnormalities[10] or brain anomalies[11] and examined its effects using histochemical methods. The reduction of CBF after BCAS was comparable between wild-type and MMP-2-null mice. The CBF reductions (wild-type versus MMP-2-null; mean±SE %, n=3 each) were 42.5±4.3% versus 39.1±3.2% (2 hours after BCAS), 38.1±4.3 versus 39.4±4.0 (3 days), 35.2±4.6 versus 33.6±6.2 (7 days), 20.8±1.4 versus 26.9±3.1 (14 days), and 11.2±3.0 versus 24.0±4.0 (30 days). In wild-type mice, MMP-2-immunoreactive glial cells increased after BCAS compared with sham-operated mice (Figure 2A and 2B). MMP-9-immunoreactive cells were not induced after BCAS in both wild-type (Figure 2C and 2D) and MMP-2-null mice (Figure 2E). Consistently, zymography using forebrain homogenates revealed only a faint band of MMP-9 in the samples after BCAS for 3 days in both wild-type and MMP-2-null mice (n=4), whereas a robust band was found in the sample from a mouse with an incidental cerebral infarction after BCAS (Figure 2G). A band of MMP-2 was detected in the samples in wild-type mice but not in MMP-2-null mice after BCAS (n=4). However, zymography using such homogenates failed to show the upregulation of MMP-2 after 3 days of BCAS; regional upregulation of MMP-2 in the WM seemed obscured.

Klüver-Barrera staining revealed that WM lesions were predominant in the corpus callosum, caudoputamen, and internal capsule but not in optic tract on day 30 after BCAS in the wild-type mice. The medial part of the corpus callosum adjacent to the lateral ventricles was most severely affected (Figure 3E). In MMP-2-null mice, such WM lesions were far less severe (Figure 3I; Table 2). The mouse model showed little damage to the visual pathway and no difference was found between the wild-type mice and MMP-2-null mice after the operation. This may be attributable to the fact that BCAS in mice induces a milder decrease in the CBF than in the rat model and maintains a residual blood flow within the common carotid arteries and its branch, the ophthalmic artery.

In the wild-type mice on day 14 after BCAS, numerous activated microglia, as visualized by immunostaining with anti-MHC class II antibodies, were found in some WM regions (Figure 3F). In addition, the number of GFAP-immunoreactive astroglia increased in these mice (Figure 3G). In the MMP-2-null mice, the number of microglia and astroglia was much fewer in the WM as compared with the wild-type animals (Figure 3J, 3K, 3P, 3Q). Thus, both WM lesions and glial activation after chronic hypoperfusion were dramatically reduced in the MMP-2-null mice. There was no difference of the number of microglia, astroglia, and IgM-positive cells in optic tract (Figure 3P).

The BBB integrity in mice subjected to BCAS was assessed by the immunostaining for IgM and EB extravasation assay. After BCAS, the number of IgM-positive cells increased in the WM of the wild-type mice (Figure 3H) as compared with the sham-operated wild-type animals (Figure 3D). Intriguingly, the IgM-immunoreactive cells significantly decreased in the WM of MMP-2-null mice after BCAS (Figure 3L and 3R). IgM-immunoreactive cells were identified as astroglia based on their colabeling with GFAP in the perivascular areas (Figure 3L through 3O). Three days after BCAS, EB apparently leaked into the perivascular area in the corpus callosum (Figure 4B) and the cerebral cortex (data not shown). This extravasation was most notable in the paramedian portion of the corpus callosum. At all time points after BCAS, no extravasation of EB could be detected in the MMP-2-null mice (Figure 4C). The estimated percent area

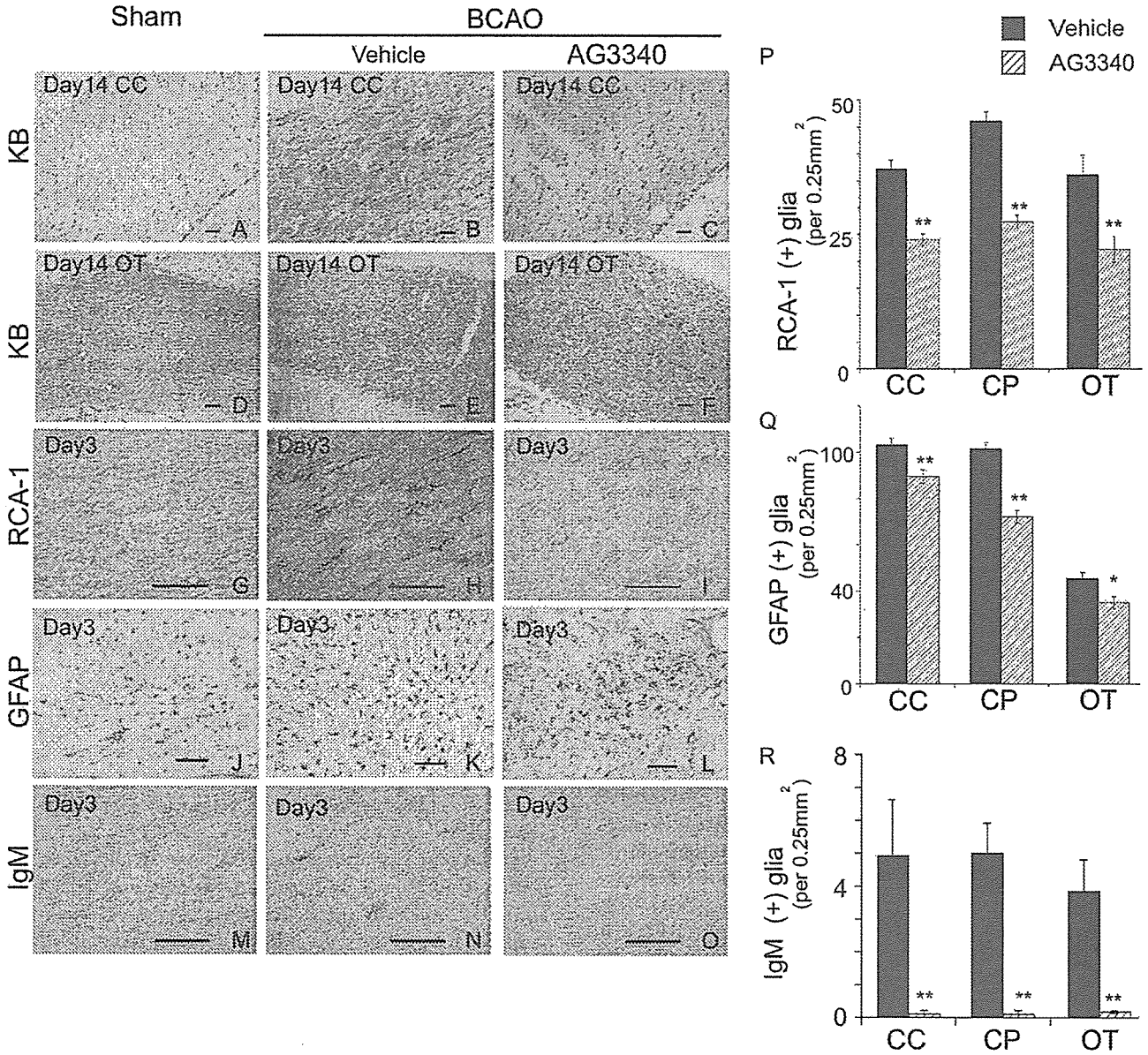

Figure 1. Histologic evaluation of the WM lesions in rats after chronic cerebral hypoperfusion with or without AG3340-treatment. A through O, Klüver-Barrera staining on day 14 (A through F; myelin sheath) or immunostaining on day 3 for Ricinus communis agglutinin-1 (G through I; microglia), GFAP (J through L; astroglia), or IgM (M through O) of the corpus callosum (A through C, G through O) and optic tract (D through F) of rats that had undergone sham operation (A, D, G, J, M) or BCAO operation, which had been treated either with vehicle (B, E, H, K, N) or AG3340 (C, F, I, L, O). Scale bar, 50 μm. (P through R) A histogram representing the density of cells immunoreactive for Ricinus communis agglutinin-1 (P), GFAP (Q), or IgM (R) in sections from the corpus callosum (CC), caudoputamen (CP), and optic tract (OT) in rats 3 days after a BCAO (n=4 each; *P<0.05, **P<0.01).

stained with EB was approximately 8% in wild-type mice after BCAS, which significantly reduced to 2% in MMP-2-null mice after BCAS (Figure 4D). Taken together, these results indicated that loss of MMP-2 alleviated BBB damage after BCAS and suggested a causative role for MMP-2 in the WM lesions after hypoperfusion.

TABLE 1. Histologic Grading of the WM Lesions in Untreated and AG3340-Treated Rats on Day 14 After BCAO

	Corpus Callosum	Caudoputamen	Optic Tract
Vehicle, N=5	1.3±045	1.4±0.54	2.6±0.55
AG3340, N=4	0.5±0.4*	0.63±0.25*	1.13±0.63*

*P<0.05.

Discussion

The synthetic MMP inhibitor AG3340 is known to inhibit several MMP family members, including MMP-2 (Ki=0.05 nmol/L), MMP-9 (0.26 nmol/L), MMP-13 (0.03 nmol/L), and MT1-MMP (0.33 nmol/L).[12] As a lipophilic, low-molecular-weight (Mr 423.5) compound, AG3340 can readily cross the BBB.[12] Using this compound, we have demonstrated that AG3340 shows protective effects against the WM lesions after chronic cerebral hypoperfusion in rats. This is consistent with our previous data using the same model, which showed a correlation of WM lesions with MMP-2 upregulation.[8] Then, AG3340 may have reduced the severity of WM lesions by inhibiting MMP-2 activation. In support of this notion,